UC Irvine

UC Irvine Electronic Theses and Dissertations

Title

Altered energy metabolism and nucleating aggregates found in normal cells as a consequence of the cell-to-cell transfer of the pathogenic polyglutamine aggregate from HD diseased cells

Permalink

https://escholarship.org/uc/item/1sg532sd

Author

Zhang, Run

Publication Date

2018

Peer reviewed|Thesis/dissertation

eScholarship.org Powered by the California Digital Library
University of California

UNIVERSITY OF CALIFORNIA,
IRVINE

Altered energy metabolism and nucleating aggregates found in normal cells as a consequence of the cell-to-cell transfer of the pathogenic polyglutamine aggregate from HD diseased cells

THESIS

submitted in partial satisfaction of the requirements
for the degree of

MASTER OF SCIENCE

in Biomedical Engineering

by

Run Zhang

Thesis Committee:
Assistant Professor Michelle Digman, Chair
Professor Enrico Gratton
Assistant Professor Tim Downing

2018

© 2018Run Zhang

TABLE OF CONTENTS

List of Figures

Acknowledgments

It is a genuine pleasure to express my deep sense of thanks and gratitude to my advisor Dr. Michelle Digman, whose guidance, patience, and encouragement during the entire process made it possible for me to get to this point. It is a great honor for me to be her student and work on such an interesting project. I am so proud of all the things I have learned and the work I have done in your lab. Words could never be enough to express my gratitude for your kindness.

In addition, I would like to thank Dr. Enrico Gratton for all the amazing instruments and software that he generously provided, for the patient explanations of fluorescence imaging techniques, for the precious and kind advices, for finding time for me in his busy schedule. He is patient, supportive and a great teacher.

I would like to thank all the LFD and Digman lab members, especially Sara Sameni for teaching me with the imaging on LSM710 and data analysis; Milka Stakic for helping me with my cell cultures; Xiantong Yang for taking time to assist me with my imaging and data analysis.

Finally, I would like to thank my family, for all their support and faith that helped me overcome all the obstacles during this entire process.

Abstract of the Thesis

Altered energy metabolism and nucleating aggregates found in normal cells as a consequence of the cell-to-cell transfer of the pathogenic polyglutamine aggregate from HD diseased cells

By

Run Zhang

Master of Science in Biomedical Engineering

University of California, Irvine, 2018

Assistant Professor Michelle Digman, Chair

Huntington's disease (HD) is a late-onset autosomal neurodegenerative disease caused by the abnormal expansion of polyglutamine (polyQ) in the Huntington gene with the mitochondrial dysfunction as an early pathological mechanism. Individuals carrying 7-35 glutamine repeats are considered normal while above 41 repetitions will always lead to HD. Compelling evidence shows that the cell-cell transfer of the mutant Huntingtin (mHTT) protein aggregates may play an essential role in the pathogenesis of HD. Most recently in our lab, we showed that energy metabolism is altered in polyQ expressing cells. Yet many questions remain: 1) Does the transfer of the polyQ aggregates occur between cells? 2) If so, do the Huntingtin proteins of normal length increase protein aggregation in normal length Huntingtin expressing cells? 3) Is there any influence in energy metabolism as a consequence of the transfer of the pathogenic polyQ aggregate from infected cells? In this research, mHTT aggregates transfer intermediated NADH fluorescence lifetime change was measured using fluorescence lifetime imaging microscopy (FLIM) coupled with phasor analysis. Results obtained

here suggest a metabolic shift from oxidative phosphorylation (OXPHOS) to more glycolytic state caused by the internalization of mHTT aggregates in HEK293 cells, which may lead to oxidative stress and cell death. Nuclear FLIM analysis shows a lifetime shift towards a lower fraction of bound NADH, which indicates a possible transcriptional dysregulation for infected cells. In addition, we performed Number and Brightness (N&B) analysis to map the oligomerization in live cells induced by mHTT aggregates. As seen in the results, there is a significant accumulation of endogenous HTT proteins after the internalization of extracellular mHTT aggregates. Altogether, the FLIM and N&B analysis used here provide a better understanding of the metabolic dysfunction and protein aggregation mediated by mHTT aggregate, which can be useful for further research in the field of neurodegenerative disease.

Chapter 1: Introduction

1.1 Protein Folding and Misfolding

Proteins are organic macromolecules essential for organism life. They are formed by amino acids bound together by the peptide bonds between the carboxyl (C-terminus) and amino (N-terminus) groups of adjacent amino acids. Different proteins with distinct sequence of amino acids have different functions such as enzymatic, immunologic, structural, and signaling.

In a cell, proteins are originally synthesized on ribosomes from the genetic information encoded in the cellular DNA. Proteins can be folded in the cytoplasm after the release from the ribosome. It is crucial for proteins to fold correctly into their compact three-dimensional structures to carry out and maintain their specific functions in the cell environment. Misfolded proteins expose some regions of structure on their surfaces that are normally hided in the interior in the native state. Thus, they are much more likely to interact incorrectly with other molecules within the environment of a cell and recruit additional monomers into aggregates by self-association[1,2].

Biological systems have developed intricate processes to ensure that proteins fold correctly. Misfolded proteins can be recognized and degraded to prevent any serious harm from happening. Molecular chaperones are proteins that facilitate protein folding by interacting with amino acid chains to avoid inappropriate associations within or between non-native peptides. There is an essential role for molecular chaperones in preventing protein misfolding since the high concentrations of these species in all cellular folding compartments. Besides protecting proteins by shielding the interactive surfaces of misfolded proteins, molecular

chaperones are also able to reverse protein misfolding and aggregating process and help them to fold correctly[3].

Misfolded proteins can be ubiquitinated by the ubiquitin-proteasome system (UPS) and can be selectively targeted and degraded by the proteasome[4,5]. A proper UPS function is particularly critical for preventing diseases that are caused by misfolded proteins. Research has shown that misfolded proteins can accumulate in neurons due to a deficient neuronal UPS activity[6].

1.2 Protein Aggregation in Neurodegenerative Disease

Increasing evidence suggests that protein aggregation and inclusion formation are common cellular mechanisms for different neurodegenerative diseases including Huntington's disease (HD), Alzheimer's disease (AD), Parkinson's disease (PD), amyotrophic lateral sclerosis (ALS) and prion diseases. Different processes such as alterations in primary structure caused by mutation, RNA modification or translational misincorporation can lead to protein aggregation[7]. Even though there are control mechanisms in the cell to prevent the formation of protein aggregates, a certain level of aggregation does occur in the cells and can result in the formation of structured, fibrillar aggregates[3]. The newly synthesized polypeptide chains are able to fold to form the folding intermediates. The folding intermediates can be either folded into or unfolded from the native polypeptides. Unstable non-native oligomeric species with different sizes and structures can be formed by these folding intermediates. This step is slow since the oligomeric species are sensitive to cleavage and clearance. The non-native oligomers can keep recruiting abnormal monomers until a stable aggregate is formed. Such aggregate can keep expanding by

incorporating with non-native monomers and oligomers or can be degraded into smaller fragments that act as aggregation nucleus and recruit abnormal molecules again[1] (Fig. 1.1). In Huntington's disease, misfolded Huntingtin proteins can be identified and labeled by antibodies or ubiquitin. However, they can still accumulate in the cells since the insufficient degradation by proteasomes[8].

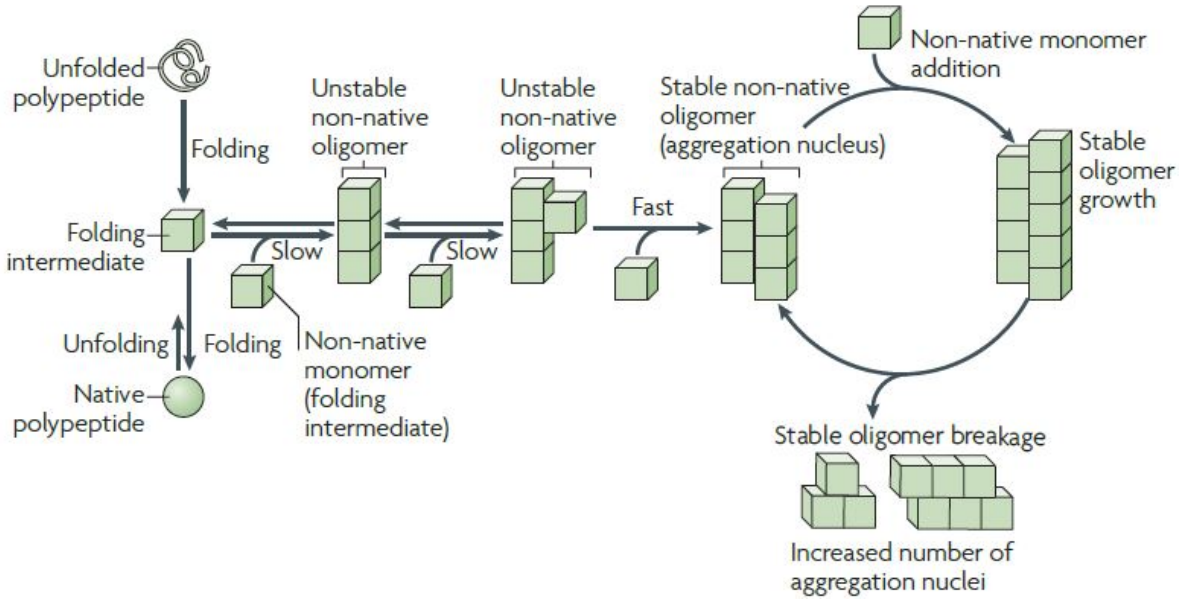

Figure 1.1: Basic mechanisms of protein aggregation[1].

1.3 Huntington's Disease (HD)

Huntington's disease (HD) is a late-onset autosomal neurodegenerative disease that causes chorea, dystonia, cognitive decline and behavioral difficulties. HD is estimated to occur in 5 to 7 people per 100,000 cases. It shows a stable prevalence in most populations of white people and a lower prevalence in Asia and Africa[9]. One of the highest rates of HD occurs in Venezuela with a prevalence of 700 per 100,000 people[10]. The condition usually appears in the middle age, with an irreversible progression of motor, psychiatric and cognitive symptoms, and

finally, lead to death within 10 to 20 years[11]. However, when the disease develops before the age of 20, the condition is called juvenile Huntington's disease[12]. An earlier emergence of the disease often results in a more rapid disease progression and a somewhat different set of symptoms including bradykinesia, rigidity, dystonia and epileptic seizures[13,14]. Choreic movements are often absent in children who develop juvenile HD[15]. Therefore, the diagnosis of juvenile HD may be difficult unless one of the parents has the fully developed disease[16].

HD is caused by an abnormal expansion of a trinucleotide (CAG) repeat within exon 1 of the Huntington gene, leading to the expansion of the polyglutamine (polyQ) stretch in the N-terminus of the Huntingtin protein (HTT). The number of CAG repeats is correlated with the severity of the disease and inversely correlated with the age of onset of disease[17]. Individuals carrying 7-35 repeats of CAG are considered as healthy. Those with 36 to 40 repeats show incomplete penetrance for HD, which means that some people with these lengths will develop HD later in adult life and some will not. Those with more than 41 repeats carry the full penetrant allele and will always develop HD[9]. Most adult-onset HD has 41 to 55 CAG repeats while juvenile-onset HD can occur with much longer CAG expansions (typically more than 70)[18].

Neuropathological change in HD is characterized by a selectivity of neuronal loss with greatest severity in the striatum and the deeper layers of the cerebral cortex[19]. Losses of 58% of the striatum and 20% of cortex were found, with astrogliosis and nuclear membrane indentation[20,21]. Striatal medium spiny neurons that contain enkephalin are much more affected in the early and middle stage of HD[22,23]. As the disease progresses, a significant volume loss occurred in the cortex, globus pallidus, and thalamus[18].

Currently, there is no drug approved that can stop or even slow down the HD progression. Treatments available to HD patients only manage symptoms and improve quality of life[24]. Researchers reported that tetrabenazine (TBZ) is the only FDA approved drug that can effectively lessen chorea in ambulatory patients specifically for HD[25]. However, many serious adverse events could happen compared to other treatments[26]. TBZ treatment should be avoided in those with a history of depression or current low mood since it can lead to severe depression[27]. The reduction of Huntingtin expression, targeted small molecule approaches and stem cell therapy are promising, because of the simple genetic mutation that causes HD, but it is still under investigation with research studies and animal models[28,29]. Thus, a more thorough understanding of the HD pathology might contribute to the identification of new treatments and therapeutic approaches discovery.

1.4 Huntingtin

Huntingtin is a completely soluble protein contains 3,144 amino acids. It is coded by Huntington's gene (IT-15 gene) which is located on chromosome 4 and is composed of 67 exons. The HTT expression is found mostly in neurons and also in the cytoplasm of most cells in the body[30]. HTT is proposed to have multiple roles in cellular biology such as cellular transport processes signaling, protection from apoptotic cell death, acting as a scaffold protein and transcriptional regulation[30,31]. HTT also has an essential role in embryonic development and reduced level of HTT leads to embryonic lethality in Huntingtin-knockout mice[32-34].

HEAT repeats are tandem repeat protein structural motif composed of two antiparallel α-helices with a helical hairpin configuration, which assembles into a superhelical structure with

a continuous hydrophobic core[35]. Sequence analysis revealed that HTT gene contains multiple HEAT repeats and a polyglutamine stretch (polyQ) is located at the N-terminus[36]. The function of HEAT repeats is still unclear, although the superhelical structure they formed often involved in intracellular transport and chromosomal segregation[37].

Exon 1 (HTTex1p) in HTT gene is consist of a cytosine-adenine-guanine (CAG) repeat corresponds to the polyQ, and a cytosine-cytosine-guanine (CCG) repeat corresponds to the polyproline (polyP) (Fig. 1.2). Mutations in exon 1 domain in the N-terminus is responsible for the toxicity and aggregation of HTT. HTT has been found to have many protein-protein interaction partners, particularly at its N-terminus, indication a scaffold function for HTT to coordinate complexes of other proteins. The toxicity of mutant N-terminal fragment of HTT is strongly supported by the interaction roles of HTT at N-terminal.

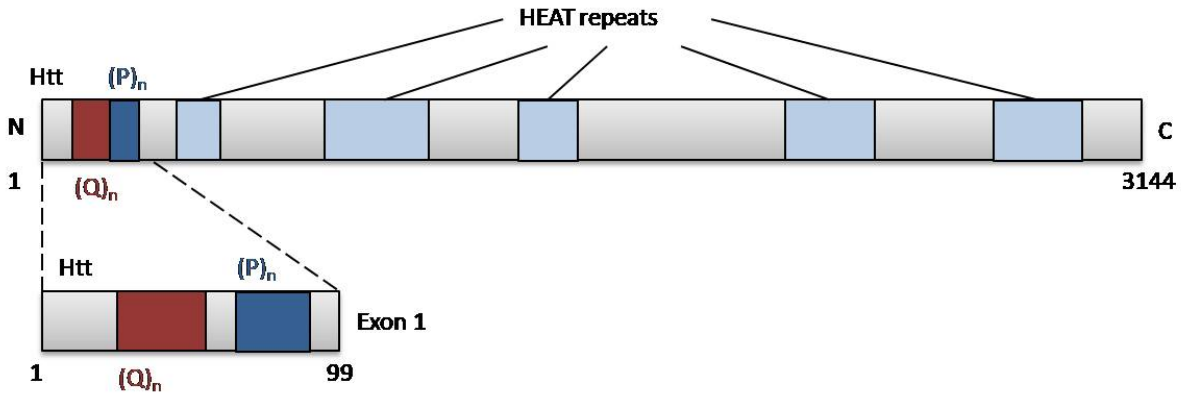

Figure 1.2: Huntingtin domain structure and Huntingtin exon1 (Httex1p). (Figure adapted from 25)

It has been shown that small N-terminal HTT fragments are sufficient to cause neurodegeneration in transgenic animals and cell death in cultured cells[38-40]. Toxicity of Httex1p with expanded polyQ has been shown in mice, flies, worms, and yeast with the same symptoms

of HD since the aggregation, subcellular localization, membrane interaction, and cytotoxicity are mediated by the first 17 amino acids of HTT protein[41,42]. It was found that N-terminal mutant HTT fragment forms aggregates in the cytoplasm while full-length mutant HTT protein is mainly diffuse in the cytoplasm of the brain cells[43-45]. Mutant N-terminal HTT fragments can also result in increased plasma membrane fluidity leading to the cell membrane defects[46]. In addition, the accumulation of transgenic N-terminal HTT fragments is found in the nucleus although they do not have functional nuclear export or import sequences[38,40]. This is possibly due to the passive diffusion of small N-terminal HTT fragments into the nucleus because of their small size.

For these reasons above, Httex1p with expanded polyQ repeat is used as a model for Huntington's disease research. In this work, we used HTT exon 1 gene with different polyglutamine sequence lengths fused with EGFP or mCherry to characterize the cell-cell transfer of mHTT aggregates and the consequent metabolic shift in the co-culture environment.

1.5 Mitochondrial dysfunction in HD

Mitochondria are double-membrane-bound organelles found in most eukaryotic organisms. The major roles of mitochondria are the production of ATP through respiration, supporting the cell signaling pathways, and maintaining control of the cell cycle and cell growth[47]. Mitochondrial dysfunctions are common symptoms in many systemic and neurodegenerative diseases due to respiratory function deficiency, large-scale mitochondrial DNA (mtDNA) rearrangements, mtDNA mutation, and excessive amounts of reactive oxygen species (ROS) production[48].

Mitochondrial dysfunction has been described as an early pathological mechanism in Huntington's disease[49]. Mitochondrial calcium defects, ATP generation reduction, and disrupted mitochondria trafficking distuption have been found with the localization of mHTT proteins in the brain[50-52]. These defects are possibly due to either a direct interaction of mHTT with the organelle or respiration and mitochondrial membrane potential modulation. Researchers found that the brain mitochondria from full-length mHTT transgenic mice have a lower membrane potential and depolarize at lower calcium loads compare to control. In addition, mitochondrial defect was also found in lymphoblast and skeletal muscle from HD patients, indicating that the mHTT induced mitochondrial abnormalities is not limited to neurons[50,53,54]. Studies also showed decreased activities of complexes II, III and IV of the electrontransport chain in HD patients' striatum[55].

Glycolysis is the metabolic pathway that converts glucose into pyruvate, generating ATP and NADH. In the presence of mHTT, the Ca^{2+} influx through *N*-methyl-D-aspartate receptors is increased and the creatine kinase(CK) activity is decreased. These effects are responsible for the decrease in ATP/ADP and phosphocreatine/inorganic phosphate (PCr/Pi) ratios[56,57] (Fig.1.3). Moreover, mHTT can also interact with glyceraldehydes-3-phosphate dehydrogenase (GAPDH) and compromise glycolysis[58].

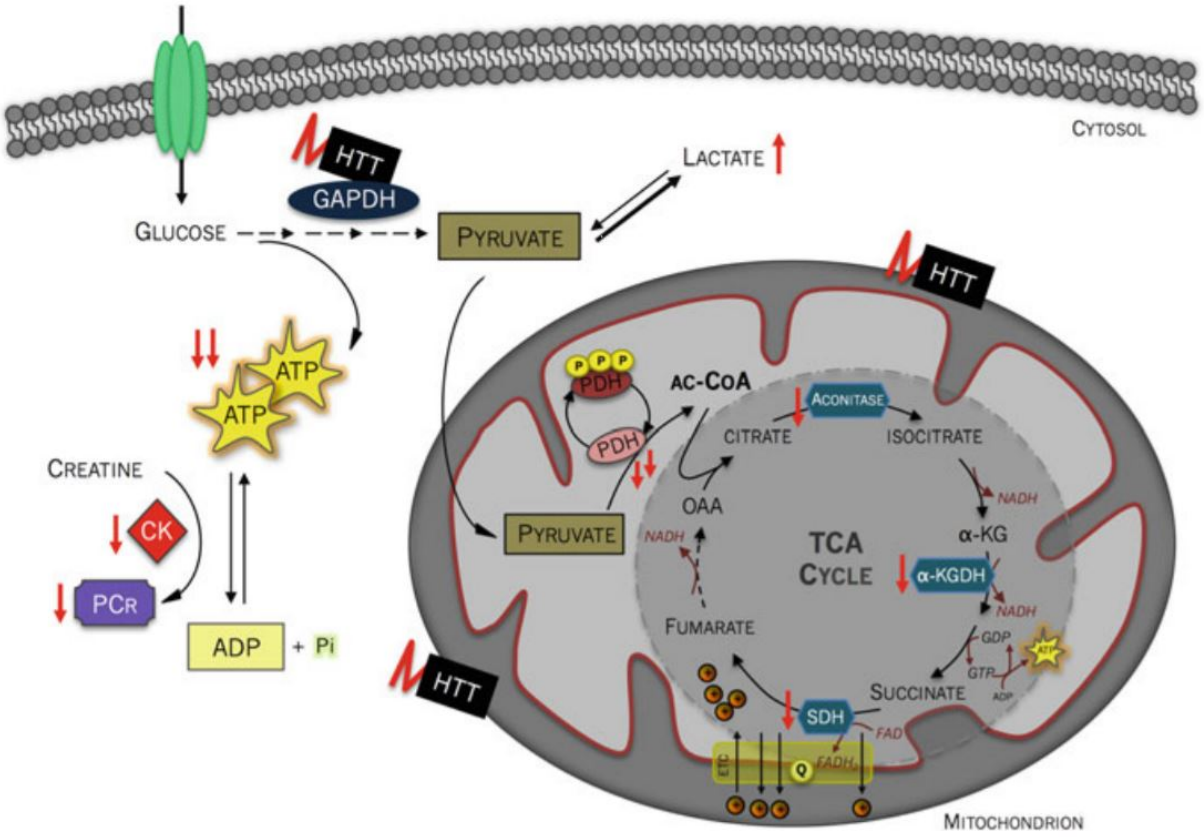

Figure 1.3: Mutant Huntingtin induces energy metabolic failure[59].

Pyruvate dehydrogenase (PDH) is a protein complex located in the mitochondrial matrix, contributes to catalyzing the irreversible pyruvate decarboxylation process from pyruvate to acetyl-CoA. With a deficiency of PDH induced by the interaction of mHTT aggregates, pruvate has been shown to accumulate in the cytoplasm and transform to lactate instead of entering the mitochondria[60]. As a result, lactate production and lactate/pyruvate ratio are increased in the striatum, cortex, and cerebrospinal fluid from HD patients[53,61,62] and brains from transgenic mouse models[63,64]. Mitochondrial defiency in HD is also decribed by the decreased activities of TCA cycle and mitochondrial respiratory chain complexes[65]. Defects in enzymes such as aconitase, α-ketoglutarate dehydrogenase (α-KGDH) and succinate dehydrogenase (SDH) in the tricarboxylic acid (TCA) cycle have been shown in central HD tissues[66,67].

Chapter 2: Aggregates Secretion and Intercellular Transfer

2.1 Transfer of Pathological Entities in Neurodegenerative Disease

The formation of inclusion bodies (IBs) initiated from disease-related misfolded proteins is characterized as the pathological hallmark of many neurodegenerative diseases. Partially folded or misfolded proteins should either be immediately refolded or degraded by the proteasome and macroautophagy. However, soluble misfolded proteins can escape degradation and accumulate together into oligomer and protein aggregates due to their exposure of hydrophobic amino acid residues[68]. Eventually, protofibrils can be formed from small aggregates by recruiting soluble monomers in the cell[69]. In Huntington's disease, intracellular aggregates and IBs can be initiated by the mutant N-terminal HTT fragments in both cytoplasm and nucleus region.

Misfolded proteins and aggregates can spread within neural systems in a prion like-fashion. Continuous secretion and internalization of aggregates are possibly responsible for the spread of pathology between neurons. Recently, the cell-to-cell transfer of pathological entities has been shown in many different neurodegenerative disease models[70-74].

2.2 Transfer of mHTT in HD

In general, monomers, oligomers and protein aggregates are released by vesicles or non-encapsulated forms such as exosomes, autophagosomes, lysosomes, and multi-vesicular bodies. Moreover, proteins can move across the membrane into extracellular space through passive diffusion or direct membrane transfer (Fig. 2.1a). Evidence demonstrates that the extracellular secretion of mHTT could propagate disease when taken up by neighboring

neurons and glia. It is still unclear how toxic mHTT is released by donor cells. Interestingly, research shows that the mHTT fibrils are able to release by axons in neurons[75]. Extracellular vesicles can be found in most of the cells in the brain. Accumulating evidence suggests that toxic mHTT fragments and its aggregates can propagate across the brain via EVs[76]. Moreover, necrosis and apoptosis may also contribute to the extracellular release of mHTT fragments[77].

The uptake of pathological entities could be mediated by either endocytosis or through direct transfer across the plasma membrane (Fig. 2.1b). Investigators have reported that α-Synuclein in Parkinson's disease (PD) could be internalized through endocytosis by neighboring cells[78-80]. In the *Drosophila* model, mHTT aggregates that are internalized by endocytosis are found to accumulate within the neurons of neighboring brain regions[81]. On the other hand, Kopito and co-workers showed the co-localization of polyQ aggregates with cytosolic markers such as HSP70, but not with markers for endosomes, lysosomes, and autophagosomes after internalization. This result indicates that polyQ aggregates are able to cross the plasma membrane through direct membrane penetration[82].

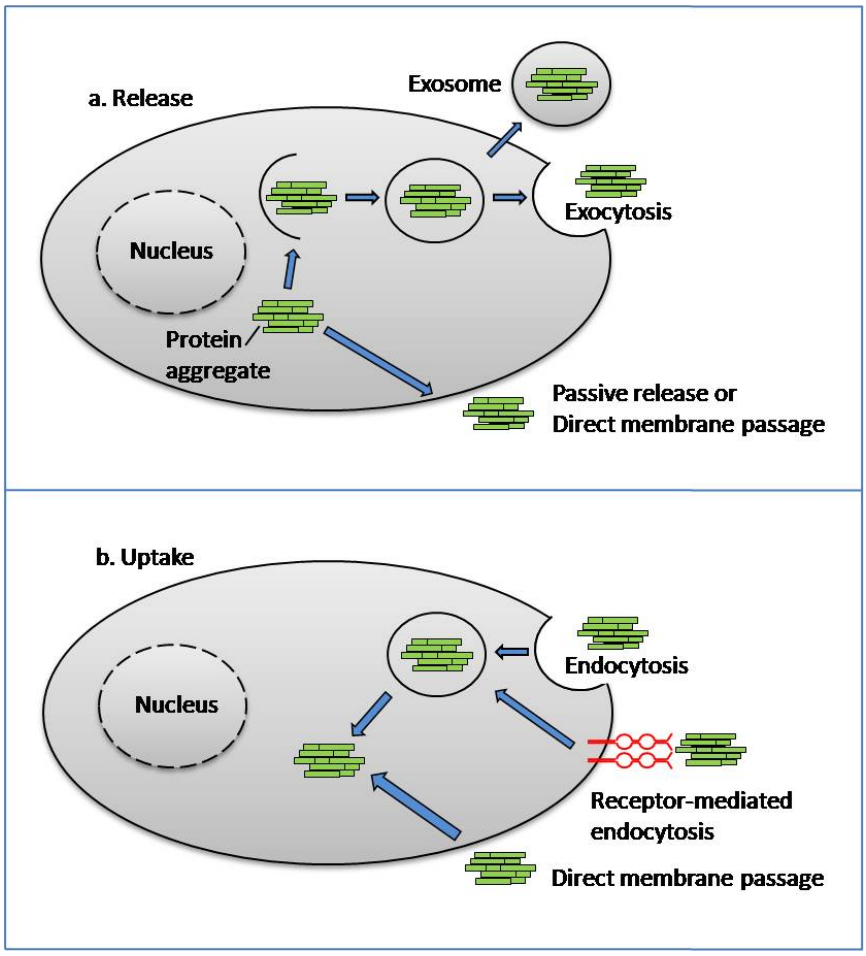

Figure 2.1: Possible mechanisms of release and uptake of aggregated protein. (a) Schematic representation to show the release of protein aggregate in cells. (b) Possible uptake mechanisms by healthy cells. (Figure adapted from 1)

Protein aggregates in neurons could travel between cells through tunneling nanotubes (Fig. 2.2)[83]. Costanzo *et al.* found mHTT aggregates in TNT-like connections between neurons and astrocytes, suggesting an important role of TNTs in mHTT transfer between primary neurons. Interestingly, they detected an increase in the number of tunneling nanotubes between CAD cells with the overexpression of mHTT fragments. This finding suggests that the formation of TNTs can be promoted by the overexpression of mHTT fragments, thus provide an efficient mechanism for aggregate transfer[84]. mHTT proteins can also transfer between neurons through synaptic connections achieved by the release of synaptic vesicles (Fig. 2.2). Botulinum

neurotoxins (BoNTs), which can block synaptic vesicle from releasing, are able to stop the transneuronal spreading of mHTT within human neurons. Thus, the mHTT aggregates' propagation is related to synaptic activities[85].

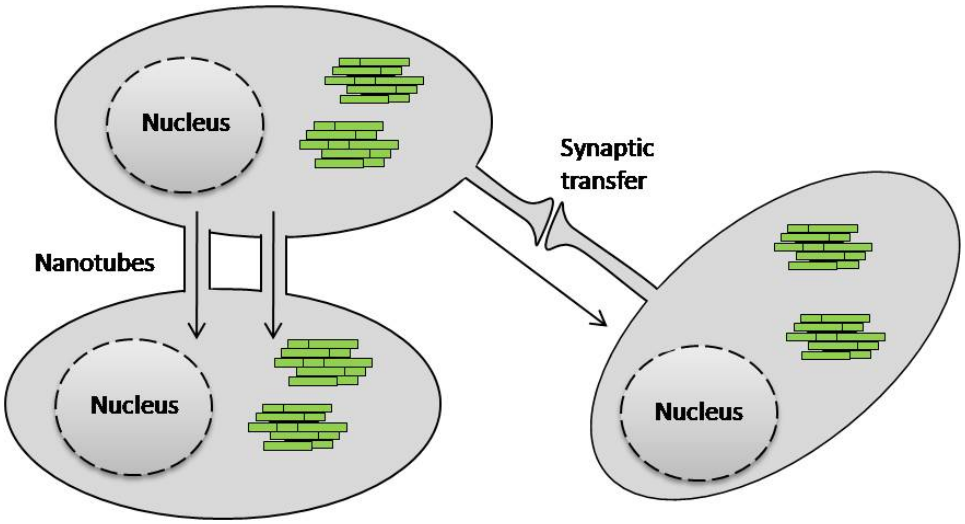

Figure 2.2: Mechanisms of aggregated protein spreading via TNTs and Synaptic transfer. (Figure adapted from 1)

In Huntington's disease, mechanisms of toxic mHTT transcellular spreading and its contribution to cell pathology are largely unknown. This is difficult to study in live cells because it is hard to observe the transfer of mHTT and at the same time study the pathological changes such as mitochondrial dysfunction. Sameni *et al.* measured the metabolic alteration in both live cells and transgenic *Drosophila* eye discs using Fluorescence Lifetime Imaging Microscopy (FLIM) with phasor approach[86]. In their experiment, they measured the fraction of free and bound forms of nicotinamide adenine dinucleotide (NADH) in both normal and HD cells. Sameni showed that there is a significant shift towards free form NADH in HD cells compared with normal cells, which indicates a shift of cell metabolism from oxidative phosphorylation (OXPHOS) to more glycolysis in HD cells. Other researchers suggest that the propagation of mHTT throughout the brain is critical to the non-cell autonomous pathology of HD[85].

With Fluorescence Lifetime Imaging Microscopy (FLIM) technique, used in this work, it is possible to measure the metabolic changes during the transcellular propagation of mutant Huntingtin. Therefore, it could be possible to determine the contribution of mHTT transfer to mitochondrial dysfunction pathology in live cells, which can be further inhibited by some treatment.

Chapter 3: Materials and Methods

3.1 Cell Culture and Transfection

Human Embryonic Kidney cell 293(ATCC® CRL-1573™) were used in all experiments because it has been widely used in cell biology research for years as their reliable growth and propensity for transfection. These cells were grown in Dulbecco's Modified Eagle Medium (DMEM) containing 10% fetal bovine serum (FBS) and 1% Penicillin/streptomycin. All cells were maintained in the cell culture incubator at 37°C with humidified 5% CO_2 and subcultured every 3-4 days.

Before experiments, cells were plated in the 6-well plate at around 70% confluency at 24 hours before transfection. Cells were then transfected with different DNA plasmids using Lipofectamine 3000 (Invitrogen, Carlsbad, CA) according to manufacturer's instruction. DNA expression plasmid used for transfection contained Human HTT gene with either 25 (normal) or 97 (expanded) copies of CAG repeat encoding polyglutamine (polyQ) fused with EGFP or mCherry at C-terminus (Httex1p 25Q-EGFP, Httex1p 25Q-mCherry, Httex1p 97Q-EGFP). These plasmids were maintained and amplified in transformed DH5-α *E.coli* using Plasmid Miniprep Kit (QIAprep® Spin Miniprep).

3.2 Confocal Imaging

HEK 293 cells transfected with DNA plasmids were imaged 12h after co-culture using Zeiss LSM710 confocal laser point-scanning microscope (Carl Zeiss, Jena, German) equipped with 488nm argon-ion laser, 561nm DPSS laser and 63× oil immersion objective (NA 1.4). Glass bottom dish with co-cultured cells were placed in the microscope incubation system kept at

37°C with 5% CO_2 and locked in the microscope heated stage maintained at 37°C throughout the imaging experiment. Fluorescence microscopy images were collected by ZEN software (Carl Zeiss, Jena, German) with 512 × 512 pixels and with a pixel dwell time of 12.61µsec/pixel and acquired using PMT detector and emission filter range 500-550nm and 580-700nm for EGFP & mCherry detection respectively. Z-stack images were collected with a Z-dimension range of 10 – 20µm. The same cells were tracked using the automatic stage positioning option between scanning. We saved the spatial coordinates position of each cell of interest and acquired images of different positions using the time interval of 20 or 30 minutes for several hours in total as a time series video.

3.3 Fluorescence Lifetime and its Measurement

3.3.1 Fluorescence Lifetime Imaging Microscopy (FLIM)

Fluorescence lifetime imaging microscopy is used as a routine technique in cell biology that maps the spatial distribution of molecules' lifetime within cells. The fluorescence lifetime refers to the average time a fluorescent molecule spends in the excited state before returning to the ground state by emitting a photon[87]. The lifetimes of fluorophores are generally ranged from picoseconds to hundreds of nanoseconds and depend on the environment condition. If a population of fluorophores is excited by a short pulse of light, the lifetime (τ) is the time required for the number of excited molecules to decrease exponentially to $1/e$ or 36.8% of the original population via fluorescence according to:

$$n(t) = n_0 e^{-t/\tau} \quad (1)$$

Since the number of molecules n is proportional to the intensity and the intensity of the emission versus time can be recorded by the camera, it is possible to study the decay of the intensity to obtain information of the lifetime (Fig3.1):

$$I(t) = \alpha e^{-t/\tau} \tag{2}$$

where $I(t)$ is the intensity at time t, α is a normalization term (the pre-exponential factor).

If the decay is a single exponential and the exciting light pulse is short relative to the lifetime of the fluorophore, then the lifetime can be determined directly from the slope of the curve. However, if the excitation pulse is wide, the measured fluorescence will not be purely exponential. In this case, some type of "deconvolution" method must be used to extract the lifetime. If the decay is multi-exponential, the relation between the intensity and time after excitation is given by:

$$I(t) = \sum_i \alpha_i e^{-t/\tau_i} \tag{3}$$

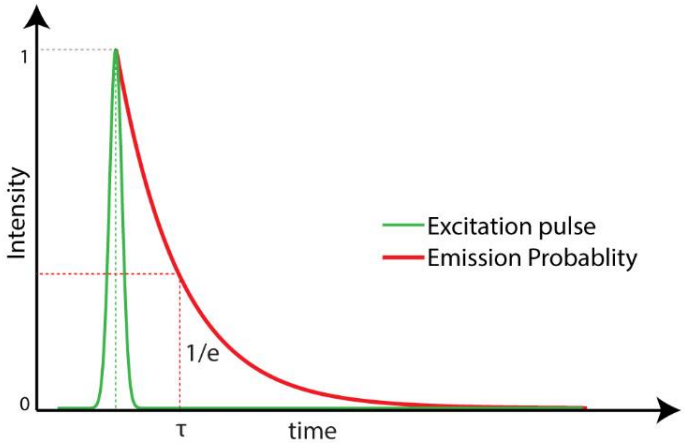

Figure 3.1: Schematic of excitation, single exponential fluorescence decay curve,and lifetime[88].

Fluorescence lifetimes have traditionally been measured using either the impulse response or the harmonic response method. In principle, both methods have the same

information content. These methods are also referred to as either the time domain method or the frequency domain method. In the time domain method, the sample is illuminated many times with a very short pulse of light, and the times at which individual photons are detected by the detector are recorded with respect to the excitation laser pulse usually by Time-Correlated Single Photon Counting (TCSPC). After enough recorded event, a fluorescence decay histogram can be built and the lifetime can be recovered by fitting the histogram with an exponential function.

In the frequency domain method, a continuous light source is used, and the intensity of this light source is modulated sinusoidally at high frequency. In this case, the modulated excitation signal for a given frequency of modulation is described by (Fig 3.2):

$$E(t) = E_0[1 + M_E \sin(\omega t)] \quad (4)$$

where $E(t)$ and E_0 are the intensities at time t and 0, M_E is the modulation factor which is related to the ration of the AC and DC parts of the signal, and ω is the angular modulation frequency given by $\omega = 2\pi f$, where f is the linear modulation frequency.

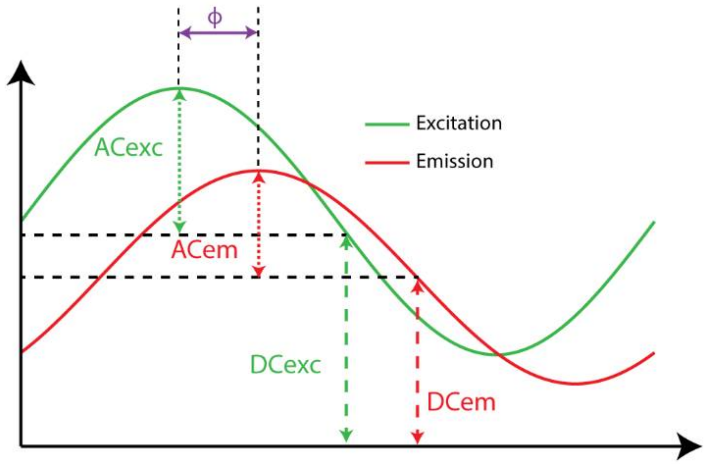

Figure 3.2: Schematic diagram of frequency domain excitation and emission signal[88].

The emission signal of the fluorophores is phase shifted relative to the exciting light due to the delay between absorption and emission. The emission frequency can be written as:

$$F(t) = F_0[1 + M_F \sin(\omega t + \phi)] \quad (5)$$

where $F(t)$ and F_0 are the intensities at time t and 0, M_F is the modulation factor for the emission signal, and ϕ is the phase delay between excitation and emission. The phase lifetime (τ_P) can be obtained by:

$$\tan \phi = \omega \tau_P \quad (6)$$

The modulation factor of the excitation (M_E) and the emission (M_F) are given by:

$$M_E = \frac{AC_{EX}}{DC_{EX}} \quad (7)$$

$$M_F = \frac{AC_{EM}}{DC_{EM}} \quad (8)$$

The relative modulation(M) of the emission is then:

$$M = \frac{(AC/DC)_{EM}}{(AC/DC)_{EX}} \quad (9)$$

The relationship between M and modulation lifetime (τ_M) is given by:

$$M = \frac{1}{\sqrt{1 + (\omega \tau_M)^2}} \quad (10)$$

The equality of τ_P and τ_M at all modulation frequencies indicates single exponential decay. However, if the fluorescence decay is multi-exponential, then $\tau_P < \tau_M$ and the value will depend on the modulation frequency[89].

3.3.2 Phasor Approach to Fluorescence Lifetime Imaging Analysis

For fluorescence lifetime data, the best way to resolve the decay at each pixel is already a difficult problem, especially while measuring lifetime from heterogeneous samples like cells, since the decay profiles are no longer single exponentials. The fitting is difficult in multi-exponential decay since it requires expertise to choose the initialization parameters and to correctly extract the information about the number and abundance of the molecular species[90]. On the other hand, it is only possible to collect light for a limited amount of time (100-200 microseconds per pixel) which results in about 1000 photons per pixel[91]. This is barely enough to distinguish a double exponential from a single exponential decay. Here we employ the phasor approach to fluorescence lifetime imaging microscopy, which provides images of molecular species by using their phasor fingerprints, without resolving and exponential fitting of the measurements. The phasor approach transforms the time delay histogram at each pixel into a phasor. If a single pixel contains more than one fluorescent molecular species, we can easily identify each molecule by their position in the phasor plot since every molecular species has their specific phasor[92].

Once the time or frequency domain FLIM data is collected, it can be transformed into a phasor plot to get the coordinates (g, s). In the case of the time domain, the values of g and s components are given by:

$$g_i(\omega) = \frac{\int_0^\infty I(t)\cos(\omega t)\,dt}{\int_0^\infty I(t)\,dt} \tag{11}$$

$$s_i(\omega) = \frac{\int_0^\infty I(t)\sin(\omega t)\,dt}{\int_0^\infty I(t)\,dt} \tag{12}$$

where $I(t)$ is the intensity at time t, ω is the angular repetition frequency of the laser. If the data is acquired in the frequency domain, the coordinates are described by:

$$g_i(\omega) = m_i \cos(\varphi_i) \tag{13}$$

$$s_i(\omega) = m_i \sin(\varphi_i) \tag{14}$$

where m_i and φ_i are the modulation and the phase shift of the emission with respect to the excitation. In case of a single exponential decay, the g and s coordinates are given by:

$$g(\omega) = \frac{1}{1 + (\omega\tau)^2} \tag{15}$$

$$s(\omega) = \frac{\omega\tau}{1 + (\omega\tau)^2} \tag{16}$$

There is a direct relationship between a phasor location and lifetime. All possible lifetime can be mapped into the phasor plot, and all possible single exponential lifetimes lie on the circle, which is *Universal Circle*. In the phasor plot (Fig 3.3a), the horizontal axis is for g, which has a value between 0 and 1. The vertical axis is for s, which has a value between 0 and 0.5. A short lifetime will fall near the point (1,0) which corresponds to $\tau = 0$, and a long lifetime will lie nearthe point (0,0) which corresponds to $\tau = \infty$. In the case of a system with two distinct single exponential species, the phasor of these two species fall individually on the Universal Circle. The phasor of all the possible combinations of these two single exponential components must be fall on a straight line joining the phasors of the two species, the positions of which are determined by the intensity weighted average of the contributions of each single lifetime species. In a system with many single exponential lifetime components, the phasor coordinates g and s are given by:

$$g(\omega) = \sum_k \frac{h_k}{1 + (\omega\tau_k)^2} \tag{17}$$

$$s(\omega) = \sum_k \frac{h_k \omega\tau_k}{1 + (\omega\tau_k)^2} \tag{18}$$

where h_k is the intensity weighted fractional contribution of the single exponential component with a lifetime τ_k.

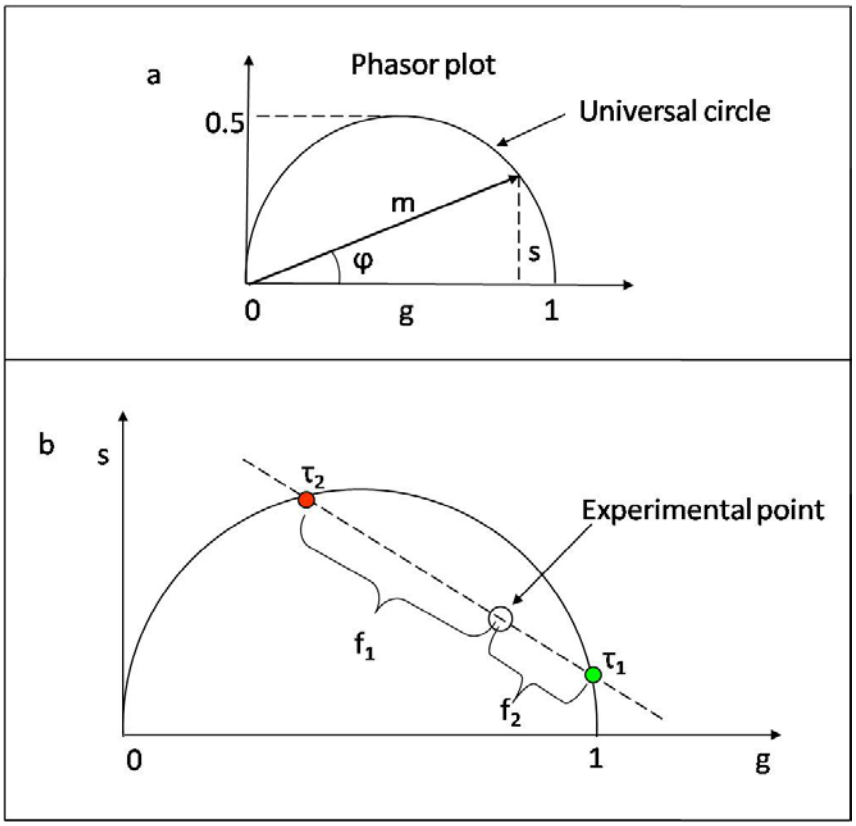

Figure 3.3: The lifetime representation using phasors. (a) Phasor plot and Universal circle. (b) Rule of the linear addition of phasors. The mixtures of τ_1 and τ_2 species must fall on the straight line between the phasors of τ_1 and τ_2 in proportion to their fractional intensity contribution.

In general, in a biological system like tissue which contains multiple fluorescent components, the overall decay is a phasor that sums all individual phasors of each fluorescence component weighted by their respective fractional contribution (Fig. 3.3b). In this case, the phasor coordinates are described by:

$$G(\omega) = \sum_n f_n g_n(\omega) \quad (19)$$

$$S(\omega) = \sum_n f_n s_n(\omega) \quad (20)$$

where f_n is the fractional contribution of each component characterized by the phasor coordinates g_n and s_n.

3.3.3 NADH FLIM

Nicotinamide adenine dinucleotide (NAD) is an important coenzyme involved in redox reactions, carrying electrons from one reaction to another in almost all living cells. NAD^+ is an oxidized form of NAD, which accepts electrons from other molecules in oxidative phosphorylation (OXPHOS). This reaction forms NADH, which is the reduced form of NAD and acts as a principal electron donor in glycolysis[93]. The ratio of the reduced and oxidized forms, NADH/NAD+ can be described as the ratio of free NADH and enzyme lactate dehydrogenase (LDH) bound NADH, free/bound ratio[94]. The fraction of free and bound form of NADH can be different in biological samples like cells and tissues depending on the location inside the cells (cytoplasm or nucleus) and the metabolic state of the cells. This free to bound NADH ratio can be an important indicator in live cells which canreflect the metabolic activity and health of these cells. A higher free/bound ratio indicates a more glycolytic state whereas a lower free/bound ratio suggesting more OXPHOS.

Autofluorescence in live cells comes from endogenous proteins and physiologically relevant fluorophores, such as collagen, elastin, NADH, hemoglobin[95]. The most important property of NADH is its autofluorescence with absorption at 340nm (740nm for two-photon

excitation) and emission at 470nm. More importantly, the fluorescence lifetimes of free NADH is significantly lower (~0.38ns) compared to protein-bound NADH (~3.4ns). These properties make it possible to distinguish between free and bound NADH using FLIM and to investigate the metabolic state of the cells without perturbing the biological system. The phasor positions of pure free and bound NADH fall on the universal circle. Any possible mixture will lie on the line (metabolic trajectory) between these two phasors in the phasor plot (Fig. 3.4). Hence, this technique has been used for metabolic imaging of tumor cell in Malignant Glioma, human embryonic stem cell and neural stem cell differentiation and so on[86,96-100].

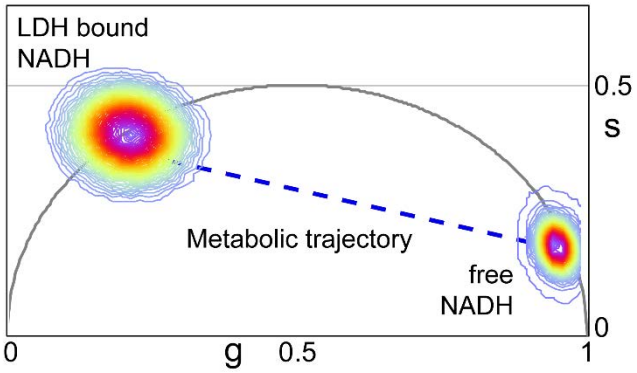

Figure 3.4: Phasor position of free and LDH bound NADH with laser repetition rate of 80MHz[88].

3.3.4 FLIM Instrumentation and Analysis

The frequency domain fluorescence lifetime imaging was achieved by Zeiss LSM710 confocal microscope (Carl Zeiss, Jena, Germany) using a 63× oil immersion objective (NA 1.4) and Titanium-Sapphire multiphoton excitation laser (Mai Tai Spectra-Physics, Newport, CA) operating at 80MHz (repetition rate of the laser). The 740nm excitation wavelength was used for NADH 2-photon excitation and a dichroic filter (690nm) was used to separate the emission signal from the excitation laser light. NADH emission signal was acquired by a bandpass

emission filter (460/80nm) and detected by external photomultiplier tube (PMT) detectors (H7422P-40, Hamamatsu Corporation, Bridgewater, NJ) and ISS A320 FastFLIM FLIMbox (ISS, Champaign, IL). Images were collected with an image size of 256 × 256 pixels and scan speed of 25.21µsec/pixel by ZEN software. FLIM data were acquired with a pixel dwell time of 25.21µsec/pixel and stopped when at least 100 - 150 counts in the brightest pixel of the image were collected or 50 - 60 frames were collected and integrated for FLIM analysis. Coumarin 6 with a known lifetime of 2.5ns was used to calibrate the phasor plot for all experiments. FLIM data were collected and further analyzed by SimFCS software developed by Laboratory of Fluorescence Dynamics, University of California, Irvine.

FLIM analysis was carried out by SimFCS software. The phasor lifetime of each pixel in the FLIM image was transformed into one point in the phasor plot. The g and s coordinates in the phasor plot were calculated from the fluorescence intensity decay curve by using Fourier transformation. Clusters of pixel values were then detected in specific regions of the phasor plot. The fraction intensity of free to bound NADH and the lifetime were evaluated using cursor by selecting the region of interest in the phasor plot. Individual cells were then masked and their average phasor values (g and s) and free to bound NADH ratio within these masked regions were calculated.

3.4 Experimental Procedure

For co-culture experiment, cells were transfected with either Httex1p 25Q-mCherry or Httex1p 97Q-EGFP for 12 hours. Different transfected cells were washed with PBS, trypsinized and transferred together onto 35mm× 10mm glass bottom dishes (MatTek, Ashland, MA)

precoated with 3µg/ml fibronectin for co-culture12 h after transfection. They were allowed to attach and grow together in the incubator for 12 hours before imaging started (Fig. 3.5).Following this, the co-culture dish with Httex1p 25Q-mCherry and Httex1p 25Q-EGFP was prepared following the same procedure before and imaged in the incubator of the microscope as the control group. Cells that express Httex1p 25Q-mCherry proteins were picked by eye using 488nm and 561nm excitation laser wavelength and cells with a medium level of expression were selected and imaged for the statistic. The same experiment was carried out for co-culture of Httex1p 25Q-mCherry and Httex1p 97Q-EGFP.25Q-mCherry expressing cells that uptook 97q-EGFP aggregates were selected for imaging. Once a handful of cells were located, their positions were saved to follow the same cell for the period of 6 to 10 hours with a time interval of 20 to 30 minutes. A stack of 20 confocal images was collected, saved and edited in ZEN software for time-lapse video.

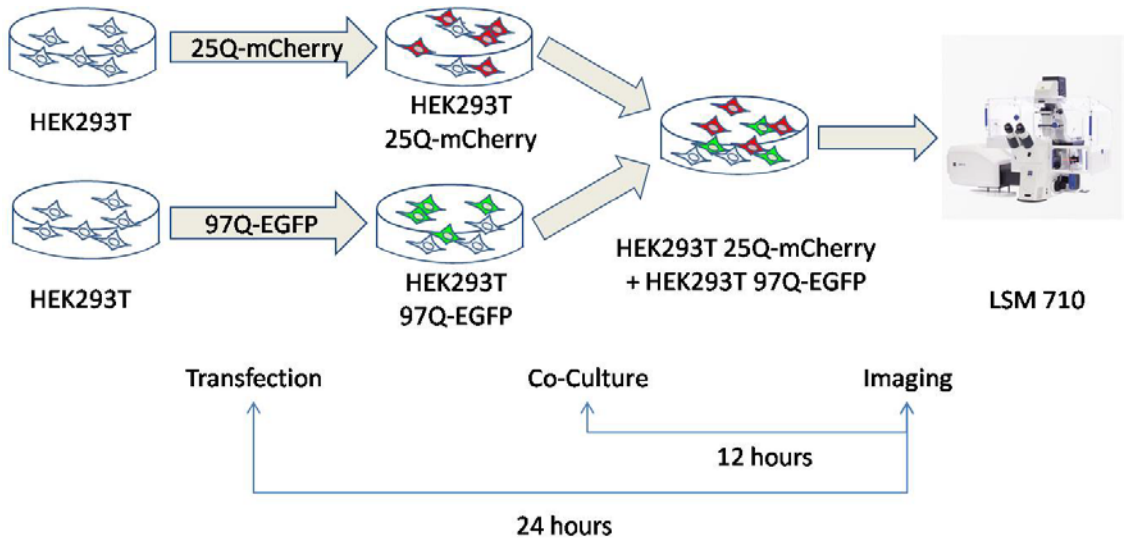

Figure 3.5: Co-culture experiment procedure.

For FLIM acquisition, prior to the imaging, FLIM images of Coumarin 6 with a known lifetime of 2.5ns were taken to calibrate the FLIM system. Different groups of co-cultured

HEK293 cells were then imaged using 740nm excitation laser wavelength for NADH 2-photon excitation. Images of 25Q-mCherry expressing cells were collected with an image size of 256 × 256 pixels and scan speed of 25.21µsec/pixel by ZEN software. FLIM data were acquired by SimFCS software with a pixel dwell time of 25.21µsec/pixel and stopped when at least 100 - 150 counts in the brightest pixel of the image were collected or 50 - 60 frames were collected and integrated for FLIM analysis.

For uptake experiment, HEK293 cells were transfected with Httex1p 97Q-EGFP plasmid for 24 hours. To purify the aggregates, cells were spun down at 45000rpmfor 20 minutes and the supernatant with mHTT aggregates was transferred into a culture dish and incubated for 24 hours. The culture dish was scanned using a microscope to make sure no cell was growing in the dish. Centrifugation and incubation were repeated if needed. Blank HEK293 cells that cultured in the glass bottom dish were then treated with 2ml culture media containing the purified mHTT aggregates and cultured in the incubator for 24 hours before imaging. Cells that uptook 97Q-EGFP aggregates were picked and imaged. Both fluorescence and FLIM images were taken using the LSM 710 system. Dishes of HEK293 cells treated with 2ml fresh culture media were prepared as the control group.

All experiments were repeated multiple times in order to obtain the reliable data and results.

Chapter 4: Results

4.1 Co-culture Study

Cells with a medium level of expression were picked for imaging. Consistency in the cell selection process is critical since overexpression of the protein can alter the results to some extent. Aggregates can be formed in cells that transfected with Htt97Q-EGFP as seen below (Fig. 4.1). The fluorescence intensity of the cell (indicated by white arrow) kept increasing from time 0 to 3.5 hours until the formation of visible aggregates (indicated by yellow arrow) between 3.5 hours to 4 hours. Figure 4.2 shows the changes of cell fluorescence intensity in cytoplasm (blue dots) with the formation of the aggregates (red dots), the mean fluorescence intensity (MFI) of the cell cytoplasm increased largely from time 0 to 210 minutes, which was possibly due to the expression of Htt97Q-EGFP protein and the formation of oligomers. With the formation of a large visible aggregate between 210 and 240 minutes, the mean fluorescence intensity of the cell cytoplasm decreased significantly. The increase in the size of aggregate and the dramatic decrease in the Htt97Q-EGFP fluorescence intensity of the cell cytoplasm was possibly due to the accumulation of Htt97Q-EGFP proteins and oligomers to the aggregate in the cell.

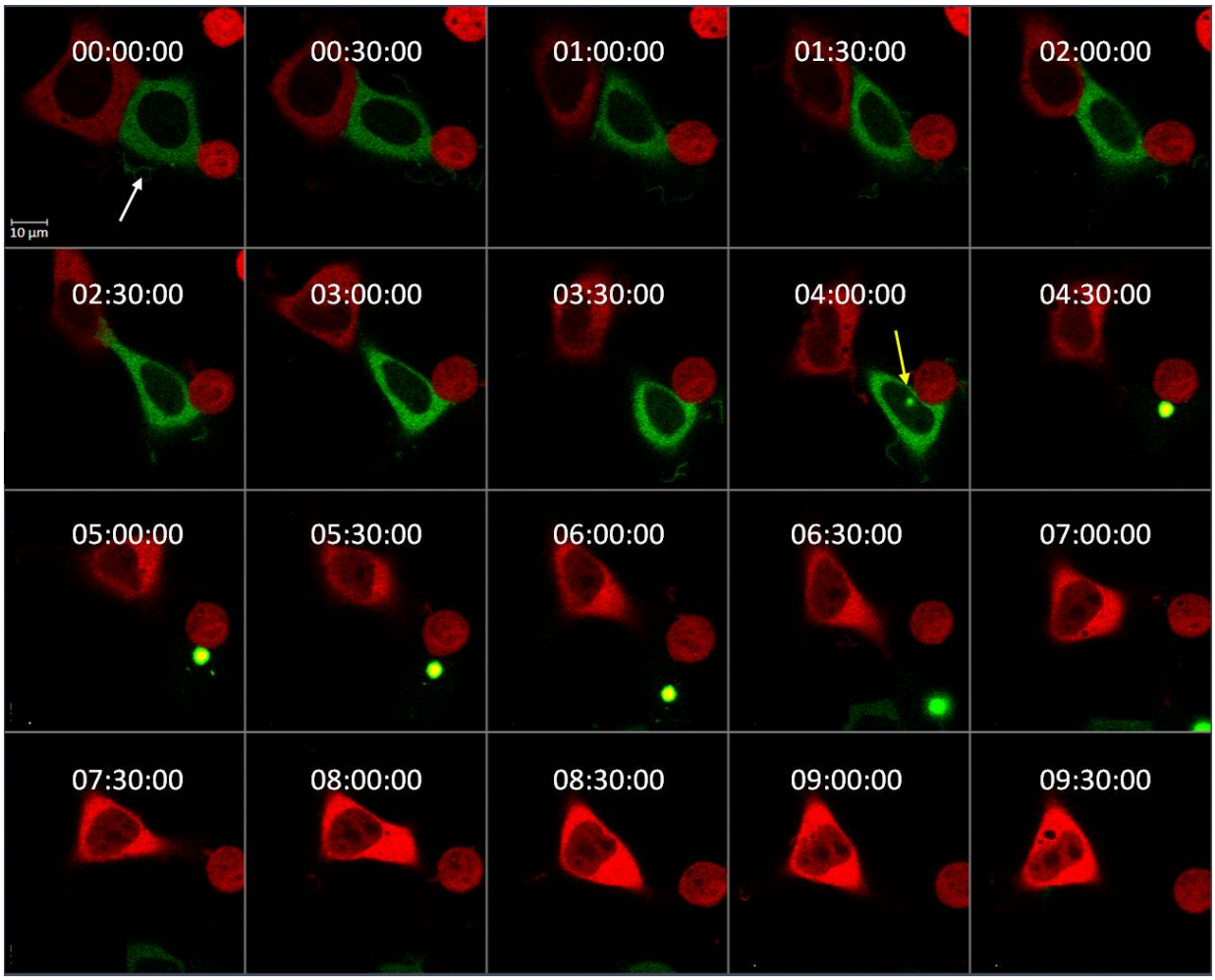

Figure 4.1: Formation of aggregates in HEK293 cells that expressing Htt97Q-EGFP proteins (Scale bar: 10µm). Time-series images for the same position were taken every 30 minutes with a total of 10 hours period.

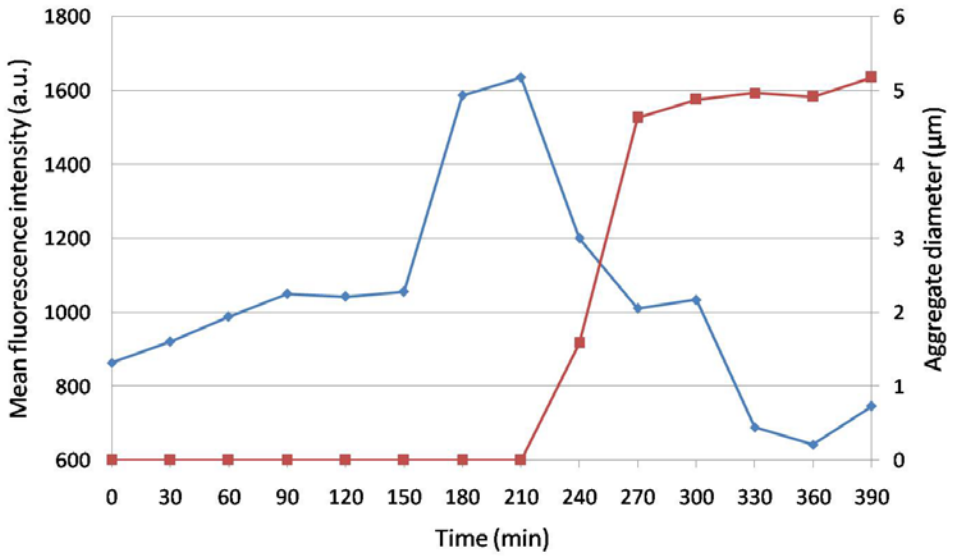

Figure 4.2: The mean fluorescence intensity in the cytoplasmic region (blue) and aggregate diameter (red) changes with respect to time. The mean fluorescence intensity of the cell cytoplasm increased at first and decreased with the growth in aggregate diameter. The timescale for this scatter plot is from 0 to 390 minutes because the cell moved out of the field of view after 390 minutes. The cytoplasm MFI and aggregate diameter are masked and measured by Icy software.

After co-culturing for 12 hours, neither the aggregate formation nor the protein transfer could be found in the co-culture of Htt25Q-mCherry and Htt25Q-EGFP transfected cells. In contrast, healthy HEK293 cells that expressing Htt25Q-mCherry proteins were able to uptake HTT97Q-EGFP aggregates. Z-stack images of the same position show that the aggregates were captured by a vesicle inside the healthy cell (Fig. 4.3).

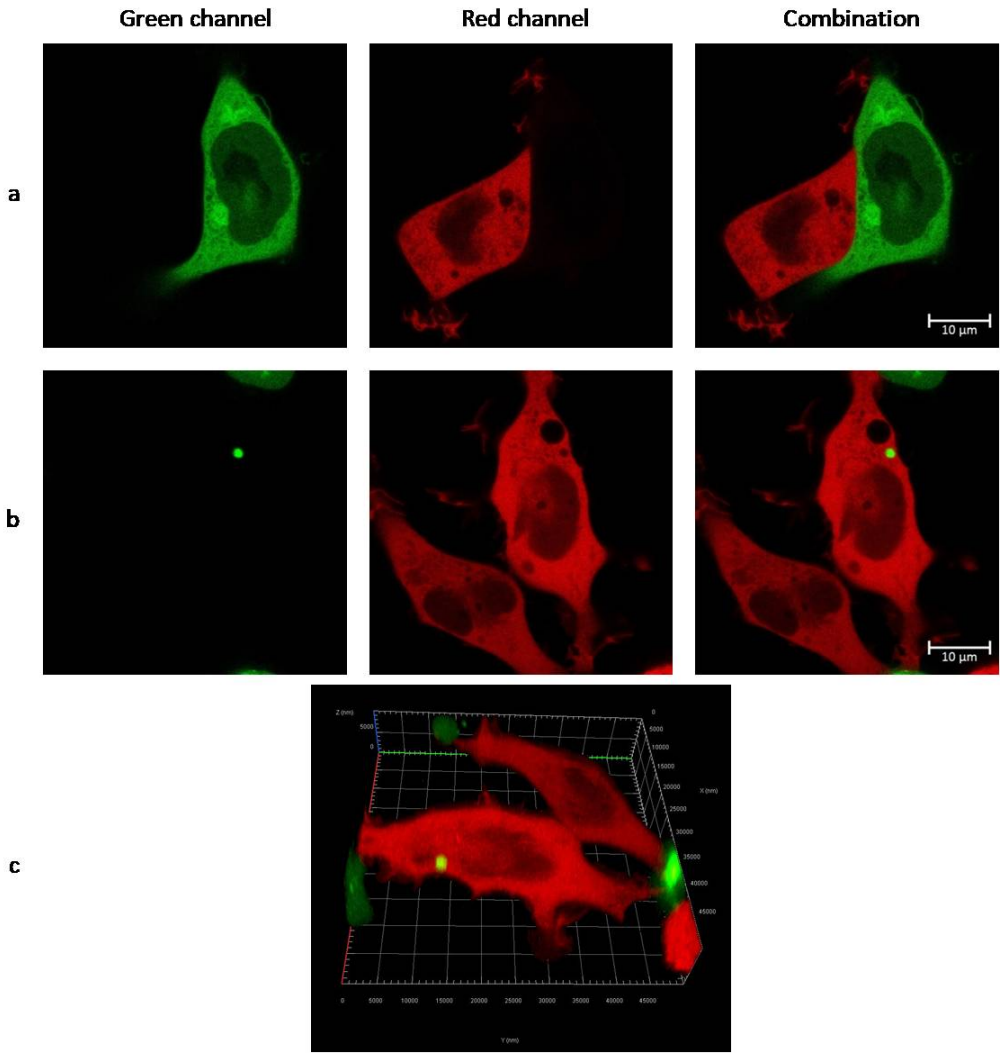

Figure 4.3: Fluorescence microscopy images representative of each experimental group (Scale bar: 10µm). (a) Co-culture of Htt25Q-mCherry and Htt25Q-EGFP expressing cells. (b) Co-culture of HTT25Q-mCherry and Htt97Q-EGFP expressing cells. (c)Image stack took at z-axis of the same position as (b).

Time-series images of the transfer group also reveal the internalization process of HTT aggregates by healthy cells (Fig. 4.4). The Htt97Q-EGFP aggregate (indicated by arrows) was captured by the elongated part of the cell (filopodia) and then was sent to the cytoplasmic region. In this case, 20 images of the same position were taken every 10 minutes with a total of 3 hours 10 minutes period.

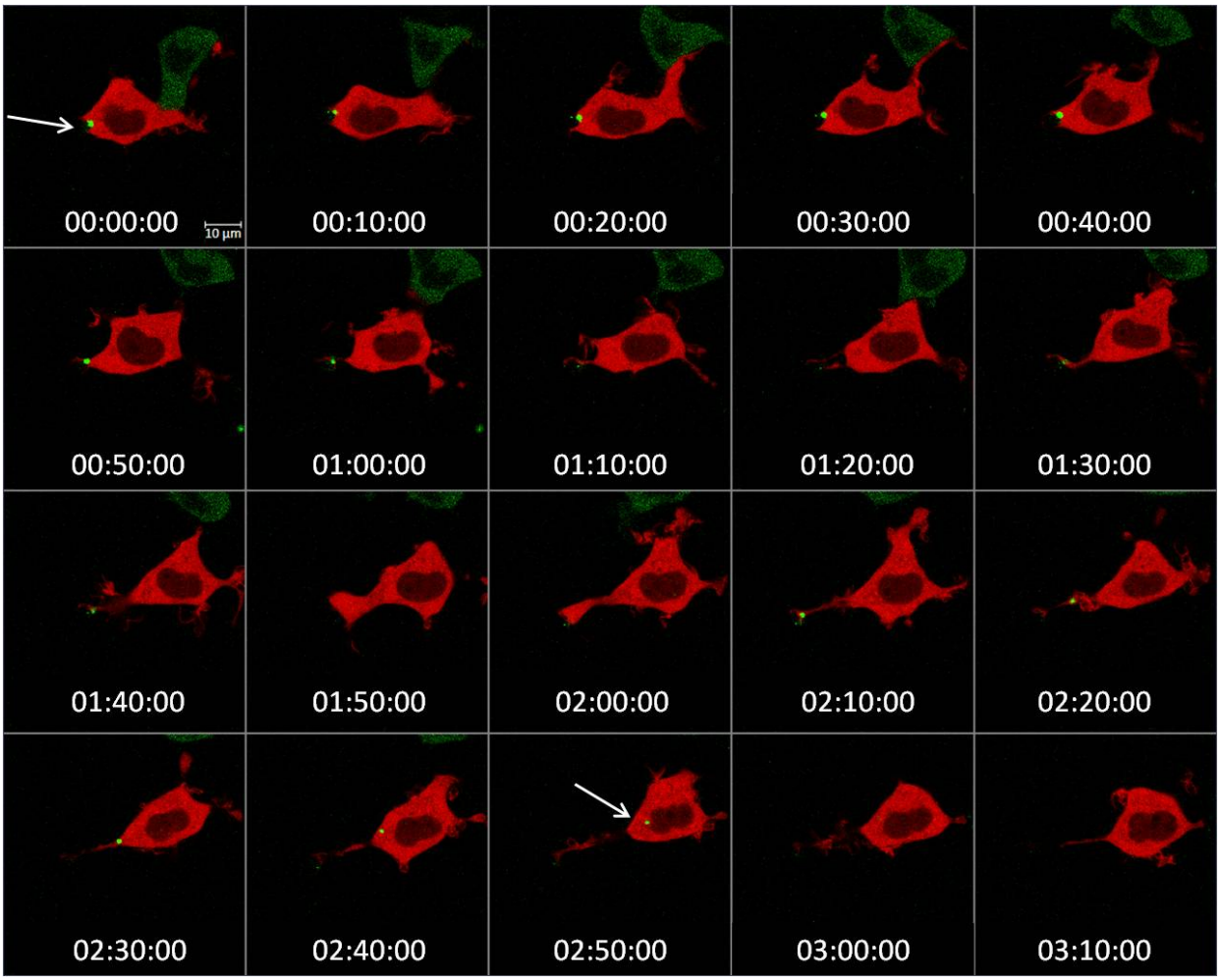

Figure 4.4: Time-series images of the aggregate internalization process (Scale bar: 10µm).

To determine the percentage of cells that formed visible Htt97Q-EGFP aggregates and the percentage of cells that were transferred with visible aggregates, we performed the tile scanning in Zen software. Using the tiles scan mode, we can acquire images that are made up of

a number of individual images (tiles), which enables us to image a lot of cells in a large field at very high resolution. The histograms of the percentage of 97Q-EGFP expressing cells that contained visible aggregates (Percentage aggregation) and the percentage of 25Q-mCherry expressing cells that contained visible 97Q-EGFP aggregates (Percentage transfer) show the aggregation and transfer efficiency in this co-culture model (Fig. 4.5). 68.1% of the 97Q-EGFP expressing cells formed visible aggregates inside the cells, while 11.8% of the 25Q-mCherry cells obtained visible 97Q-EGFP aggregates within 24 hours after transfection or within 12 hours after co-culture.

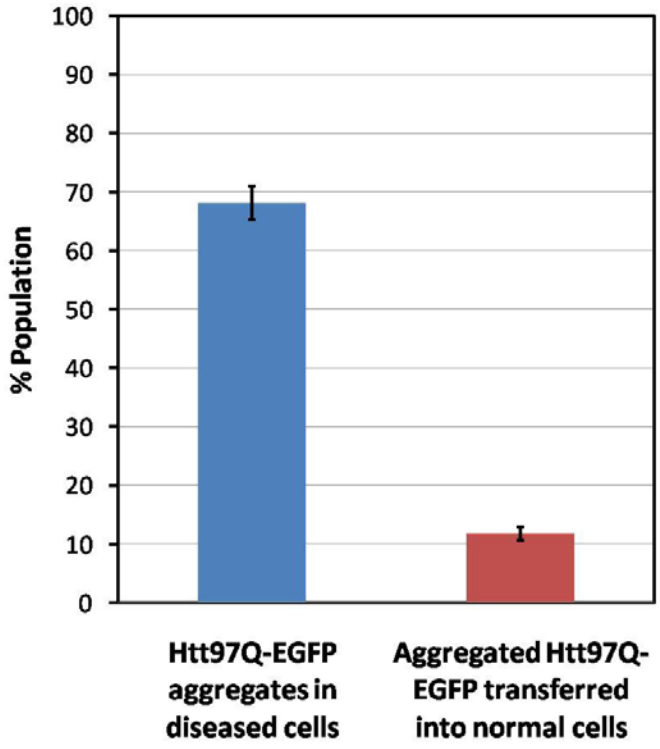

Figure 4.5: Percentage aggregation and percentage transfer revealed by tile scan counting. N=433 cells were scanned for percentage aggregation and N=279 cells were scanned for percentage transfer. The standard deviation was calculated from the mean data for all different positions.

4.2 FLIM results

We performed NADH FLIM experiment on Htt25Q-mCherry expressing HEK293 cells that co-cultured with either Htt25Q-EGFP or Htt97Q-EGFP cells. We show that the relative ratio of free to bound NADH increases on average when cells are transferred with 97Q-EGFP aggregates, which indicates a shift of ATP production from OXPHOS to glycolytic metabolism. Phasor approach in FLIM described in the previous chapter has been used to transform the fluorescence decay at each pixel in the FLIM images into a single point in the phasor plot.

Figure 4.6 shows the simultaneous intensity of EGFP and mCherry excited at 488nm and 561nm wavelength respectively, and NADH autofluorescence intensity excited at 740nm wavelength by two-photon excitation, for Htt25Q-mCherry expressing cells co-cultured with Htt25Q-EGFP or Htt97Q-EGFP expressing cells. The color in the lifetime maps in panel c corresponds to the fluorescence lifetime distribution of the cursors in the phasor plots shown in panel d. Our result shows a significant shift in both g and s coordinates value and NADH lifetime which indicates a transformation from protein bound form to free form of NADH in Htt25Q-mCherry expressing cells that uptakes the Htt97Q-EGFP aggregates compared to Htt25Q-mCherry expressing cells co-cultured with Htt25Q-EGFP expressing cells.

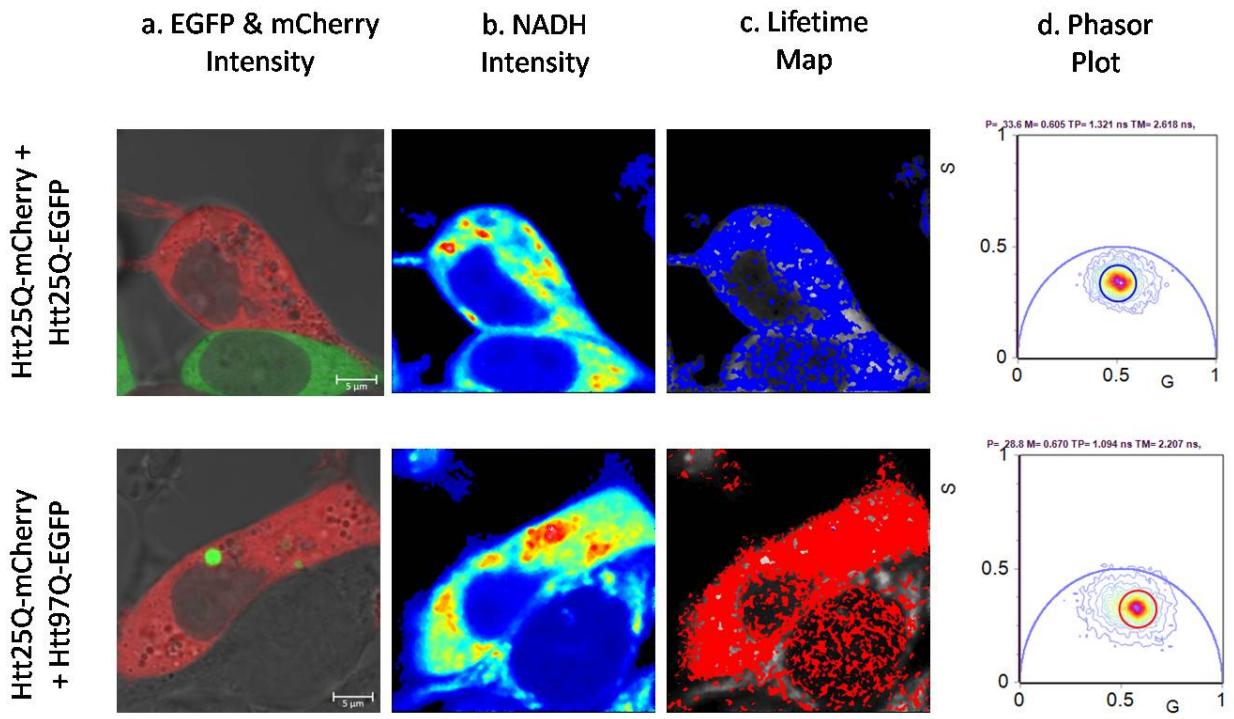

Figure 4.6: FLIM detects a shift of metabolism toward glycolysis when Htt25Q-mCherry expressing cells uptake HTTexon1 aggregates (Scale bar: 5µm). (a) Confocal images obtained using 488nm and 561nm laser to excite EGFP and mCherry respectively. (b) NADH autofluorescence intensity image obtained with 740nm two-photon excitation. (c) NADH lifetime maps colored according to the cursors in the phasor plots in panel (d).

Two distinct populations of NADH FLIM signature and significant changes in the fraction of bound NADH have been identified in both nucleus and cytoplasmic region corresponding to Htt25Q-mCherry expressing cells in normal and disease condition. Htt25Q-mCherry expressing cells that were transferred with Htt97Q-EGFP aggregates were carefully picked to make sure the aggregates were inside the cell. In the transfer group, a decreased fraction of bound NADH in both cytoplasm and nucleus indicates the metabolic defects and a lower nuclear activity (Fig. 4.7). Each point in the plot (a) and (c) represents the average lifetime plotted in the phasor coordinates. By using the mask in SimFCS software, the cytoplasmic or nucleus region for each cell is selected and the *g* and *s* values and fraction of bound NADH are calculated.

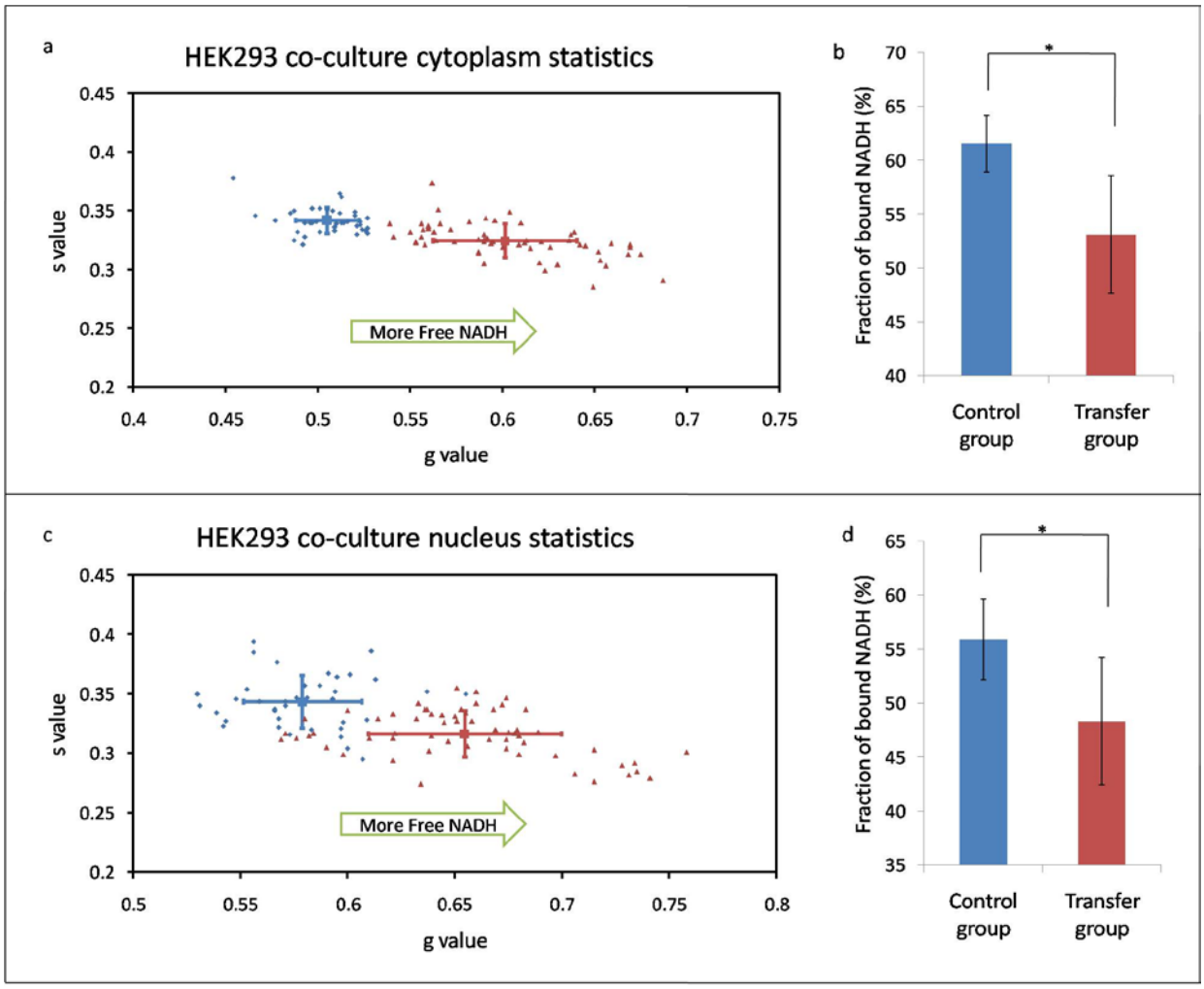

Figure 4.7: NADH FLIM phasor signature and fraction of bound NADH in cytoplasm and nucleus region. Blue dots and bars represent Htt25Q-mCherry expressing cells co-cultured with Htt25Q-EGFP expressing cells (N=39). Red dots and bars represent Htt25Q-mCherry expressing cells (with visible Htt97Q-EGFP aggregates inside) co-cultured with Htt97Q-EGFP expressing cells (N=60). (a) Scatter plot of NADH FLIM signature in cytoplasmic region for control and transfer group ($p=6.1\times10^{-28}$). (b) Bar graph represents the average fraction of bound NADH for individual cells are calculated from the distance along the trajectory on the phasor plot from completely free NADH to completely bound NADH. (c) Similar scatter plot for nucleus statistics ($p=4.3\times10^{-17}$). (d) The fraction of bound NADH in nucleus region. * $p < 0.001$.

To confirm this observation, we performed FLIM on HEK293 cells with 2ml isolated Htt97Q-EGFP aggregates treatment and HEK293 cells treated with 2ml fresh media as a control. HEK293 cells were prepared without any transfection and the preparation of purified Htt97Q-EGFP aggregates have been described in chapter 3. EGFP was excited at 488nm and NADH

autofluorescence was excited and measured using 740nm laser wavelength. In agreement with the co-culture experiment results, cells can uptake Htt97Q-EGFP aggregates. A significant shift in both *g* and *s* values and NADH lifetime were measured in cells with the internalization of Htt97Q-EGFP aggregates relative to the normal cells (Fig. 4.8).

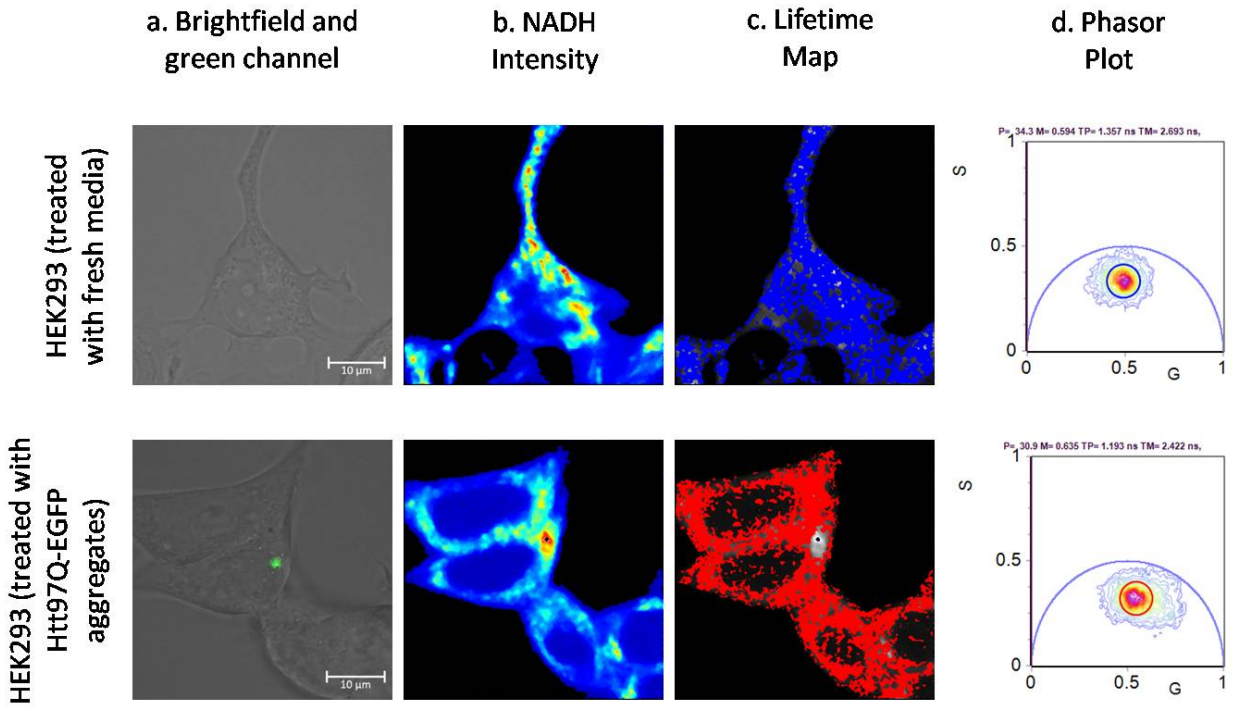

Figure 4.8: The metabolic shift toward glycolysis was detected by FLIM when HEK293 cells uptake Htt97Q-EGFP aggregates (Scale bar: 10µm). (a) Confocal images obtained using a 488nm laser to excite EGFP. (b) NADH autofluorescence intensity image obtained with 740nm two-photon excitation. (c) NADH lifetime maps colored according to the cursors in the phasor plots in panel (d). Cells are representative of each group.

Similarly, a lower fraction of bound NADH has been identified in both nuclear and cytoplasmic region in HEK293 cells with the internalization of Htt97Q-EGFP aggregates relative to normal HEK293 cells (Fig. 4.9). Together, the data suggested a distinct difference in NADH signatures between normal and Htt97Q-EGFP transferred HEK293 cells.

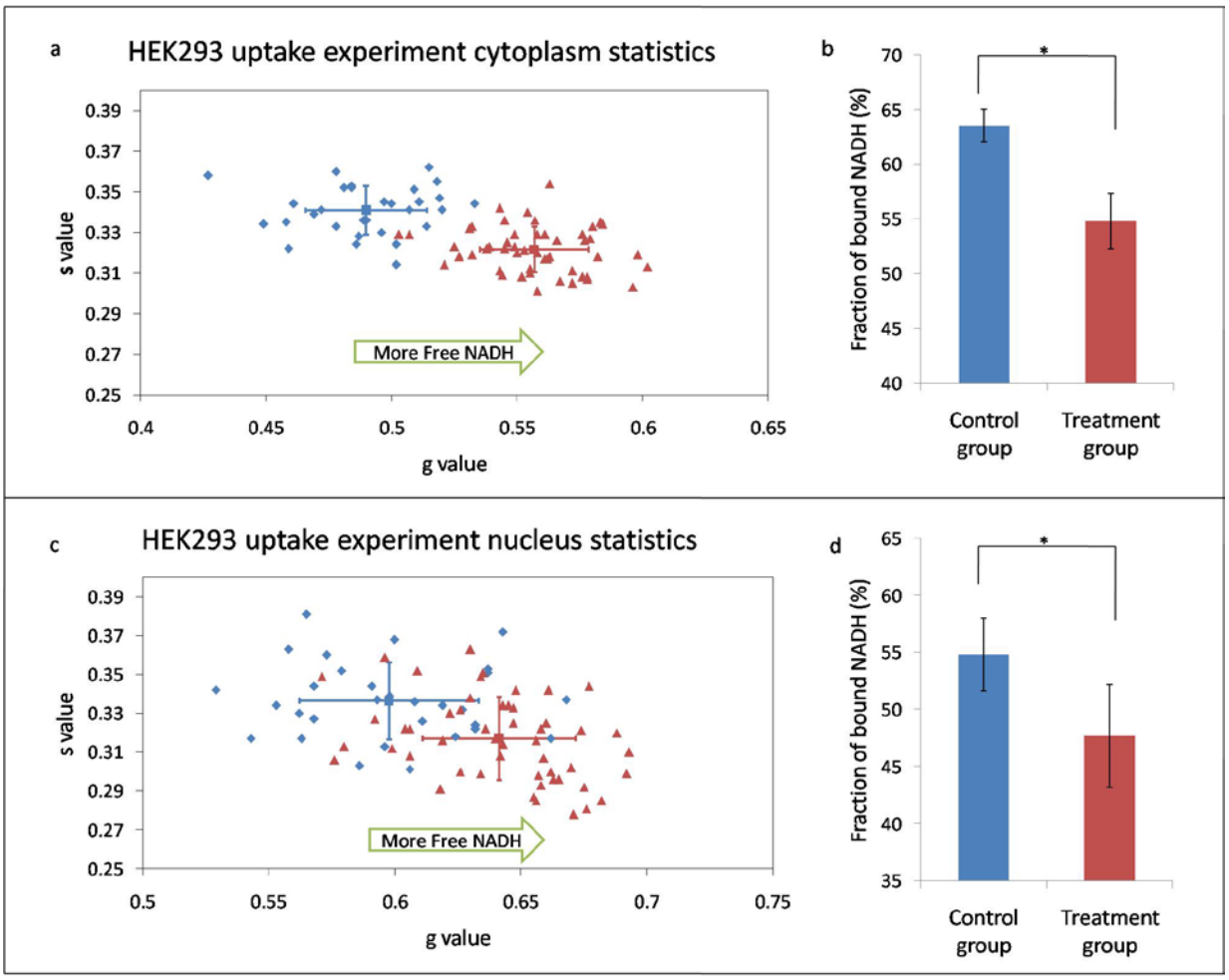

Figure 4.9: NADH FLIM phasor signature and fraction of bound NADH in cytoplasm and nucleus region in uptake experiment. Blue dots and bars represent HEK293 cells with 2ml fresh culture media (N=30). Red dots and bars represent HEK293 cells (with visible Htt97Q-EGFP aggregates inside) treated with 2ml Htt97Q-EGFP aggregates (N=51). (a) Scatter plot of NADH FLIM signature in cytoplasmic region for control and aggregates treatment group ($p=3.4\times10^{-18}$). (b) Bar graph represents the average fraction of bound NADH for individual cells are calculated from the distance along the trajectory on the phasor plot from completely free NADH to completely bound NADH. (c) Similar scatter plot for nucleus statistics ($p=3.4\times10^{-7}$). (d) The fraction of bound NADH in nucleus region. * $p < 0.001$.

To determine if the distinctions persisted with the internalization of other particles, FLIM was applied to HEK293 cells with 2µl yellow-green fluorescence beads treatment. The yellow-green beads (Invitrogen, Eugene, Oregon) used in this experiment have a mean diameter of 1µm, which is similar to the Htt97Q-EGFP aggregate. 1µl yellow-green beads with a

concentration of 3.6×10^7 beads/ml were diluted in 1ml PBS and agitated in the ultrasonic water bath for 50 minutes to eliminate all possible aggregates. No significant differences were found between HEK293 cells with yellow-green beads internalization and blank HEK293 cells in the NADH FLIM signature and fraction of bound NADH for both nucleus and cytoplasmic region (Fig. 4.10).

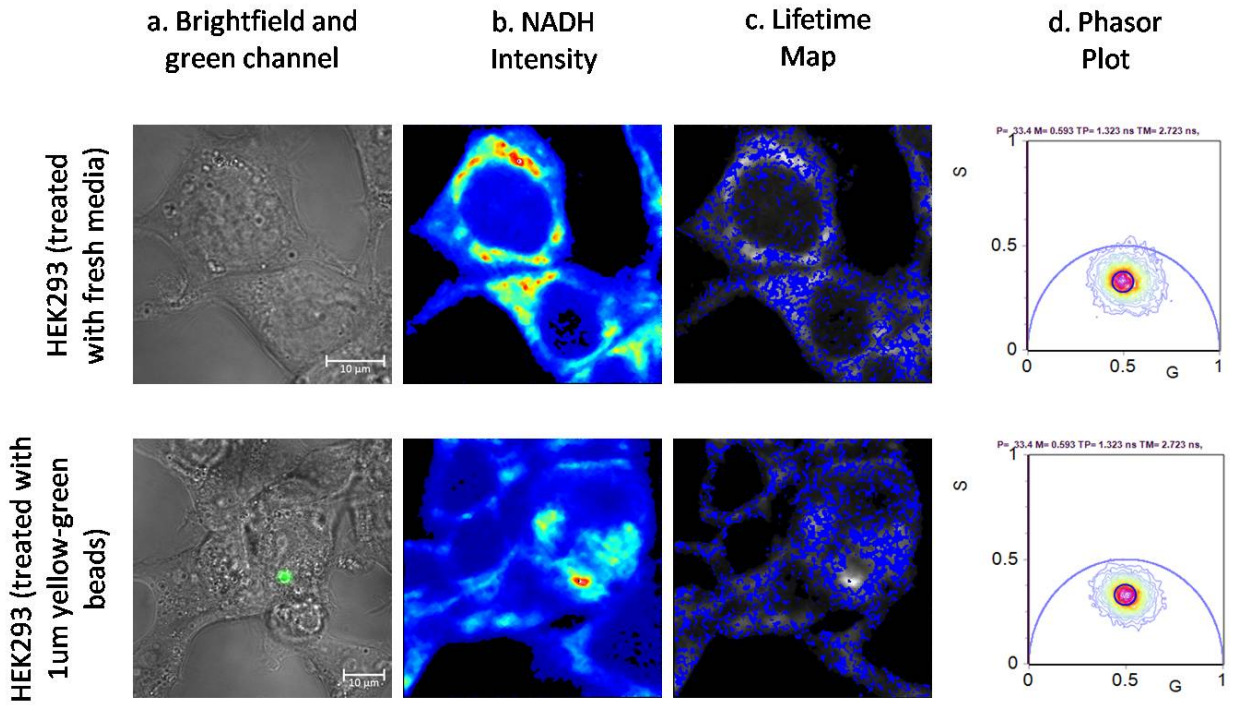

Figure 4.10: No metabolic shift was detected by FLIM when HEK293 cells uptake 1µm yellow-green beads (Scale bar: 10µm). (a) Confocal images obtained using a 488nm laser to excite the fluorescence of yellow-green beads. (b) NADH autofluorescence intensity image obtained with 740nm two-photon excitation. (c) NADH lifetime maps colored according to the cursors in the phasor plots in panel (d). Cells are representative of each group.

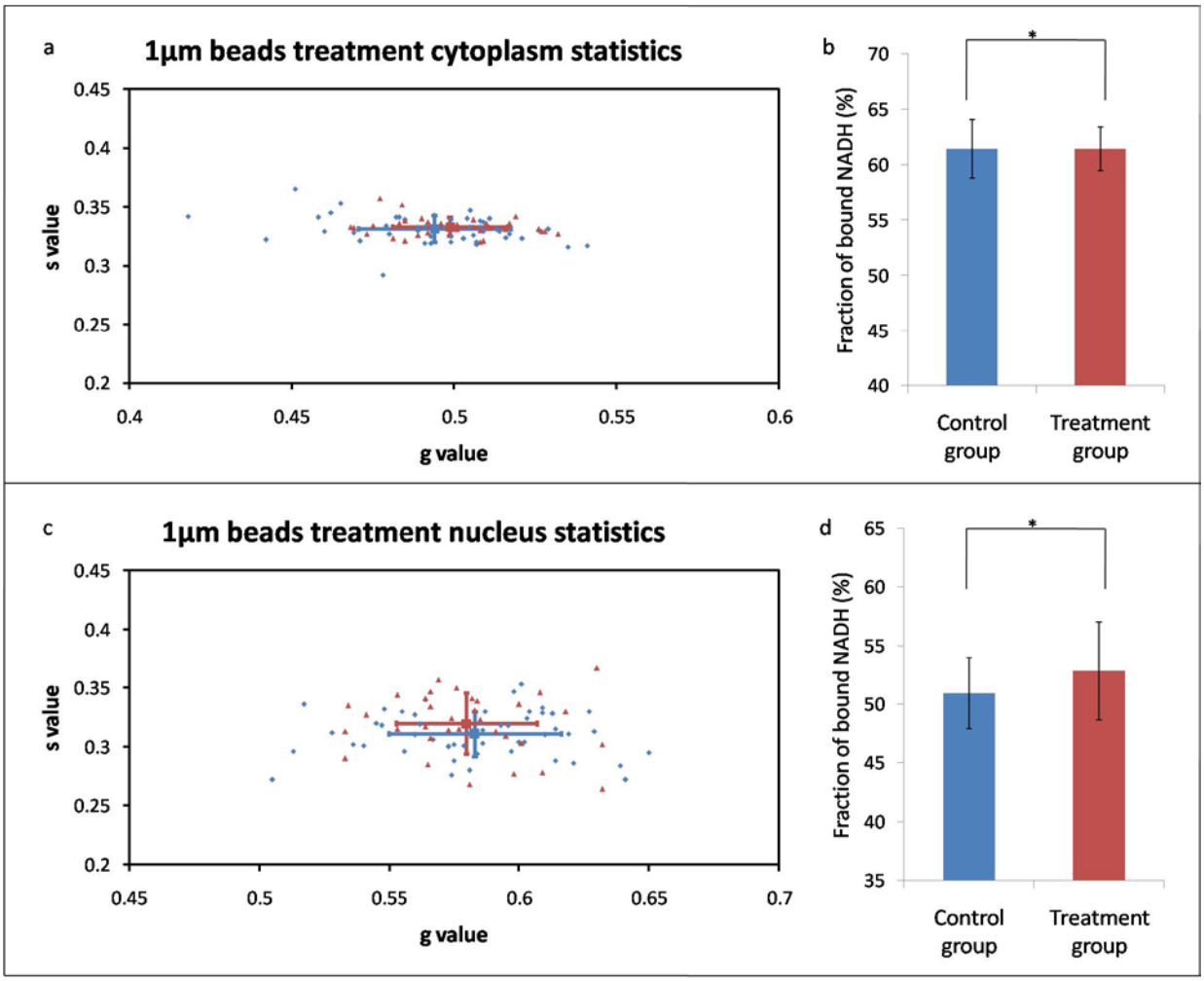

Figure 4.11: NADH FLIM phasor signature and fraction of bound NADH in cytoplasm and nucleus region in yellow-green beads treatment experiment. Blue dots and bars represent HEK293 cells with 2µl fresh culture media (N=51). Red dots and bars represent HEK293 cells (with visible yellow-green beads inside) treated with 2µl diluted yellow-green beads (N=33). (a) Scatter plot of NADH FLIM signature in cytoplasmic region for control and beads treatment group (p=0.15). (b) Bar graph for fraction of bound NADH. (c) Similar scatter plot for nucleus statistics (p=0.32). (d) The fraction of bound NADH in nucleus region. * $p > 0.05$.

Although cells can uptake 1µm yellow-green beads that treated in the culture media, the FLIM signature of the cells doesn't have a significant change relative to normal HEK293 cells (Fig. 4.11). This result indicates that the uptaking activity itself doesn't have a role in metabolic shift observed before. The internalization of Htt97Q-EGFP aggregates for normal HEK293 cells is

responsible for the metabolic shift towards glycolysis and the decrease of the fraction of bound NADH.

4.3 Discussion

Understanding the influence of aggregate transfer in the pathogenesis of Huntington's disease plays a critical role in HD research. In this thesis, frequency-domain fluorescence lifetime imaging microscopy (FLIM) was employed to measure the changes in the fluorescence lifetime of NADH. As seen in the results, it is evident that there is a significant metabolic shift towards glycolytic state after the internalization of mHTT aggregates.

Research has shown that no aggregate can be formed in Htt-25Q transfected cells, the majority of the Htt-25Q proteins are monomers[101]. In contrast, the mHTT aggregates can be formed in cells that transfected with Htt97Q-EGFP plasmid and transferred normal cells co-cultured in the same environment. The value of mean fluorescence intensity (MFI) for the cytoplasmic region of the cell gradually increased from 863.05 to 1054.66 from time 0 to 150 minutes, followed by a large increase from 1054.66 to 1634.81 within the next 60 minutes. This increase in cytoplasmic MFI is possibly due to the overexpression of Htt97Q-EGFP proteins and the formation of oligomers which are normally brighter than monomeric protein. With the formation and enlargement of a large visible aggregate and several small aggregates after 210 minutes since the imaging start, the MFI of the cell cytoplasm decreased significantly from 1634.81 to 745.83. This is possibly due to the accumulation of mHTT proteins and oligomers to the aggregate in the cell. It is interesting to see the relationship between the fluorescence intensity changes and the formation of aggregates, thereby providing new evidence for the

recruitment of mHTT protein and the aggregation in HD. The experiments with co-culture model were carried out to study the mHTT aggregate cell-cell transfer and its influence in the metabolic dysfunction in HD. Tile scan counting result shows that 68.1±2.83% of the Htt97Q-EGFP expressing cells formed visible aggregates at 24 hours after transfection, while 11.8±1.16% of the normal cells obtained visible Htt97Q-EGFP aggregates within 12 hours after co-culture. This result confirms the effectiveness and efficiency of the co-culture model that we employed for mHTT protein aggregation and transfer study. On observation after a longer time period, most of the cells are dead and detached.

For FLIM imaging in co-culture condition, FLIM identified a lower fraction of bound NADH in both cytoplasmic and nucleus region for Htt25Q-mCherry transfected HEK293 cells with the internalization of Htt97Q-EGFP aggregates compared with control group(Fig. 4.7). The fraction of bound NADH for individual cells is calculated from the distance along the trajectory on the phasor plot from completely free NADH to completely bound NADH. The fraction of bound NADH for the cytoplasm of Htt25Q-mCherry expressing cells co-cultured with 25Q-EGFP cells is 61.5±2.60%. However, when Htt25Q-mCherry expressing cells are co-cultured with Htt97Q-EGFP cells and transferred by their aggregates, the bound NADH fraction is decreased to 53.1±5.47%. These significant changes in NADH fluorescence lifetime and free to bound ratio of NADH indicate a shift in ATP production from oxidative phosphorylation to more glycolysis that can lead to an increase in oxidative stress and eventually cell death. In addition, nucleus NADH analysis on Htt25Q-mCherry cells with the mHTT aggregates uptake indicates decreased bound NADH fraction compared to normal. Such a shift toward increased free NADH in the nucleus indicates transcriptional dysregulation in mHTT transferred cells which is crucial in HD

pathogenies. To confirm that the distinct phasor FLIM signatures observed in co-culture experiment are related to the uptake of mHTT aggregates and not an artifact of protein overexpression or fluorescence labeling, Htt97Q-EGFP aggregates were isolated and treated to blank HEK293 cells without any transfection and fluorescence labeling. In agreement with the co-culture results, a lower fraction of bound NADH was detected in both nuclear and cytoplasmic region in HEK293 cells with the uptake of Htt97Q-EGFP aggregates compare to normal condition. Similarly, the metabolic shift toward glycolysis has also been identified by FLIM after the internalization of mHTT aggregates, which further supported the metabolic dysfunction in healthy cell induced by the uptake of mHTT aggregates in HD. To determine whether this significant metabolic shift was induced by mHTT aggregates or the uptake activity was responsible for this shift, we performed NADH FLIM on HEK293 cells with yellow-green beads internalization. The preparation and concentration of 1μm yellow-green beads were mentioned before. Data acquisition and analysis were carried out in a similar fashion. However, results showed the same NADH signature and a fraction of bound NADH between the control group and yellow-green beads treatment group for both cytoplasmic and nuclear region ($p > 0.05$) (Fig. 4.11). Based on these results, the significant metabolic shift towards glycolysis and a decreased fraction of bound NADH for “infected” cells induced by the cell-cell transfer and uptake of the mHTT aggregates strongly suggest that the passage of aggregated pathogenic proteins between cells may contribute to the pathogenesis of Huntington’s disease.

4.4 Conclusion and Future Directions

Although the underlying mechanism that affects the propagation of Huntington's disease is still under investigation, compelling evidence indicates that the cell-cell transfer of toxic mHTT aggregates may play an essential role in neurodegeneration in HD. From this research, we have visualized the formation of Htt97Q-EGFP aggregates in disease cells and the cell-cell transfer of Htt97Q-EGFP aggregates to healthy cells. We used the autofluorescence lifetime of NADH as an intrinsic biomarker for measuring the metabolic perturbation in cells transferred by mHTT aggregates. Results obtained here indicate a metabolic shift from OXPHOS to more glycolytic state induced by the internalization of expanded Huntington repeats mHTT aggregates in HEK293 cells. Such a shift may indicate depletion of ATP production and an increased oxidative stress in mHTT aggregates affected cells and can eventually lead to cell death, which may explain the progressive neurodegeneration in Huntington's disease progression. Furthermore, nuclear FLIM analysis for HEK293 cells after the internalization of mHTT aggregates indicates transcriptional dysregulation which is important to understand in HD research. Overall, these results suggest that the cell-cell transfer and internalization of mHTT aggregates from HD cells to neighboring healthy cells are responsible for the metabolic shift toward glycolysis in HD progression.

In Huntington's disease research, the ability to measure the metabolic changes in a non-invasive manner and at the single cell level would be highly beneficial to understand the role of mHTT aggregates transfer in metabolic dysfunction of HD. To our knowledge, this study is the first to apply FLIM to measure the metabolic change in the progression of HD. This tool can also be used for similar neurodegenerative diseases such as Alzheimer's, Parkinson, ALS, and etc.

We expect the results of this work to be a precursor for future study using neuronal cells. Further investigations are needed to apply this research method in neuronal cells which are much more physiologically relevant to the real case. This research can be also extended to in vivo imaging of fresh brain tissue samples, which may provide much more detailed information regarding the metabolic shift in live tissues. In addition, the significant metabolic shift that we demonstrated here could be a powerful tool for possible HD drug screening.

Chapter 5: N&B Analysis in Protein Aggregation

5.1 Background

Protein misfolding and aggregation are the causes of several neurodegenerative diseases which affect an increasing number of people. The mechanism of protein aggregation has been studied in detail[101], while how monomeric HTT proteins in normal cells react to extracellular mHTT aggregates still remains unknown. As explained before, the mHTT protein aggregate has a prion-like mechanism which can elongate by the recruitment of monomeric HTT proteins and can be released into intracellular space or transferred directly into healthy cells. However, important questions on the cytotoxicity induced by extracellular aggregates and possible aggregation mechanisms in "infected" cells are still unanswered.

Recent studies have shown that the extracellular fibrillar polyglutamine peptide aggregates can be internalized by mammalian cells in culture and are able to selectively recruit soluble cytoplasmic proteins[82]. This result suggests that the internalized mHTT aggregates in "infected" cells may be capable of nucleating the aggregation of endogenous normal HTT proteins. To observe this specific aggregation mechanism in live cells, methods to detect and localize aggregates of different sizes are needed. In this way, it would be possible to understand the processes involved in the pathogenesis of Huntington's disease.

One of the major issues for this study is the differentiation of monomers and oligomers. This is difficult to study in live cells since monomers and oligomers are present at the same time during aggregation. However, we employed the Number and Brightness (N&B) analysis in this work, which makes it possible to measure all of the species and localize them during their formation in live cells. These experiments observe the aggregation mechanism of the HTT

protein inside the cells after the internalization of extracellular mHTT aggregates, which is necessary to understand the pathogenesis of Huntington's disease and can provide new strategies for the treatment of this disease.

5.2 N&B Analysis

5.2.1 Introduction

The Number & Brightness (N&B) analysis is an image correlation spectroscopy (ICS) based fluctuation method to detect the oligomerization of aggregate in cells[102]. It provides a single pixel resolution map of molecular number and aggregation by calculating the average and variance of the intensity distribution at each pixel in fluorescence images captured by laser scanning microscopes (LSM). With this information, it is possible to distinguish pixels with many dim molecules from pixels with few bright molecules. If two pixels have the same average intensity but different variance compared to the mean value, the larger is the variance, the fewer molecules are contributing to the average (Fig. 5.1).

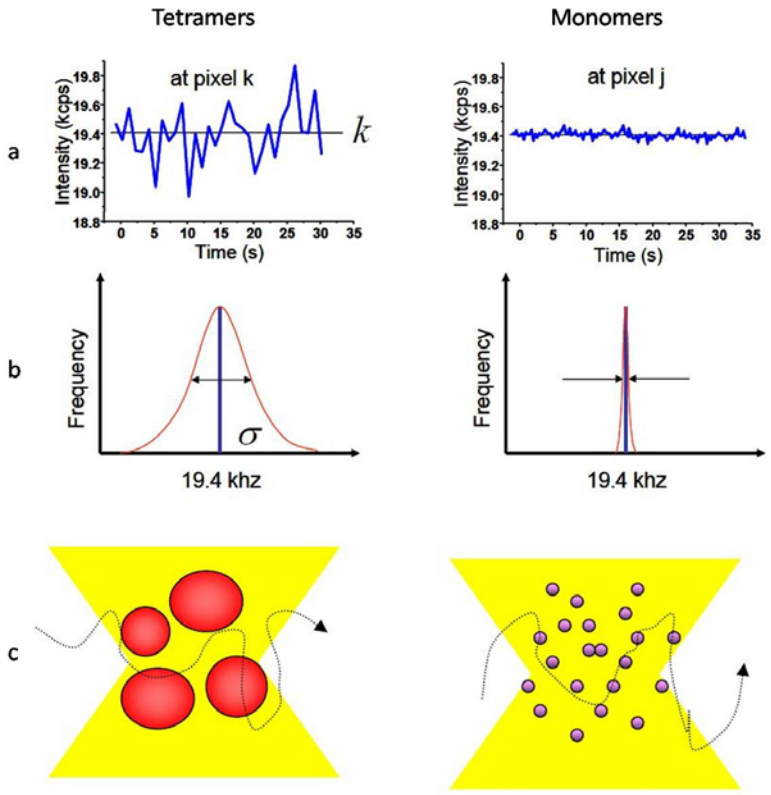

Figure 5.1: Scheme of the different distributions of intensity. (a) Fluctuations in intensity with respectto time for pixel k and j. (b) Histogram of counts corresponding to (a).(c) Observation volume for tetramers and monomers.

This analysis provides a map of apparent number of molecules (N) and brightness (B) for each pixel in the image. If a stack of K images is acquired, the average intensity $\langle k \rangle$ and the variance σ^2 in each pixel are described by:

$$\langle k \rangle = \frac{\sum_i k_i}{K} \tag{21}$$

$$\sigma^2 = \frac{\sum_i (k_i - \langle k \rangle)^2}{K} \tag{22}$$

where k_i is the intensity in the$i$ frame.

Then the apparent number of molecules N and brightness B can be calculated by:

$$N = \frac{\langle k \rangle^2}{\sigma^2} \tag{23}$$

$$B = \frac{\langle k \rangle}{N} = \frac{\sigma^2}{\langle k \rangle} \tag{24}$$

In the N&B analysis, the variance contains two terms, the variance due to the particle number fluctuation (σ_n^2) and the variance due to the detector count statistics noise (σ_d^2).

$$\sigma^2 = \sigma_n^2 + \sigma_d^2 \tag{25}$$

$$\sigma_n^2 = \varepsilon^2 n \tag{26}$$

$$\sigma_d^2 = \varepsilon n \tag{27}$$

$$\langle k \rangle = \varepsilon n \tag{28}$$

where ε is the true molecular brightness and n is the true number of molecules.

The variance due to the particle fluctuations depends on the square of the molecular brightness and will have a $B > 1$. The variance of the immobile fraction, the autofluorescence and that of the detector is proportional to the intensity of these components and in this case, $B = 1$. The average intensity is the product of the molecular brightness times the average number of particles. By substituting these definitions in the equation for the apparent number of molecules N and brightness B, we can get:

$$N = \frac{\langle k \rangle^2}{\sigma^2} = \frac{\varepsilon n}{\varepsilon + 1} \tag{29}$$

$$B = \frac{\sigma^2}{\langle k \rangle} = \frac{\varepsilon^2 n}{\varepsilon n} + \frac{\varepsilon n}{\varepsilon n} = \varepsilon + 1 \tag{30}$$

It is easy to calculate the true number of molecules n and the true molecular brightness ε from the above equations.

If an analog detector is used, the fluorescence intensity at one pixel is due to the contributions of fluctuating particles plus a constant background fraction ($offset$) which is an additional term contributes to the average intensity. In this case, the average intensity and the variance are given by:

$$\langle k \rangle = \frac{\sum_i k_i}{K} = S\varepsilon n + offset \tag{31}$$

$$\sigma^2 = \sigma_n^2 + \sigma_d^2 = S^2\varepsilon^2 n + S^2\varepsilon n + \sigma_0^2 \tag{32}$$

where S is the factor which converts photons into digital level, $offset$ is the detector offset, and σ_0^2 is the readout noise of the detector.

Thus, by simple algebra, the N&B equations become:

$$N = \frac{(\langle k \rangle - offset)^2}{\sigma^2 - \sigma_0^2} = \frac{\varepsilon}{\varepsilon + 1} n \tag{33}$$

$$B = \frac{\sigma^2 - \sigma_0^2}{(\langle k \rangle - offest)} = S(\varepsilon + 1) \tag{34}$$

The values of S , $offset$, and σ_0^2 for the analog detector can be calculated by measuring and fitting the dark counts histogram with a Gaussian and an exponential decay as shown in Fig. 5.2.

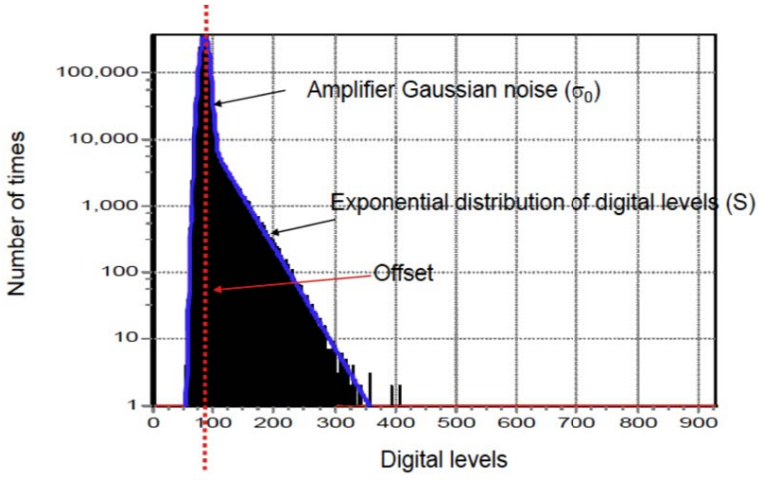

Figure 5.2: Dark counts histogram for an analog detector[101].

Overall, with this analysis, it is possible to localize and differentiate different species in cells inreal time and make a quantitative analysis of the aggregation in the co-culture system.

5.2.2 Experimental Procedure

For N&B analysis in the co-culture experiment, Httex1p 25Q-mCherry andHttex1p 97Q-EGFP plasmids were used to transfect HEK293 cells. Different transfected cells were washed with PBS, trypsinized and transferred together onto 35mm× 10mm glass bottom dishes (MatTek, Ashland, MA) precoated with 3μg/ml fibronectin for co-culture 12 h after transfection. They were allowed to attach and grow together in the incubator for 12 hours before imaging started. Dishes with mCherry orHttex1p 25Q-mCherry plasmids transfected cells were prepared and imaged in the incubator of the microscope as the control group. Cells that express Httex1p 25Q-mCherry proteins (with the internalization of Htt97Q-EGFP aggregates) were picked by eye using 488nm and 561nm excitation laser wavelength and cells with a medium level of expression were selected and imaged at 561nm wavelength with 0.5% laser power for the statistic.

5.2.3Microscope Setup and N&B analysis

The data acquisition for N&B analysis was achieved by Zeiss LSM710 confocal microscope (Carl Zeiss, Jena, Germany) using a 63× oil immersion objective (NA 1.4). Glass bottom dish with co-cultured cells were placed in the microscope incubation system kept at 37°C with 5% CO_2 and locked in the microscope heated stage maintained at 37°C throughout the imaging experiment. The mCherry protein was excited at a wavelength of 561nm using a

DPSS laser set to 0.5% laser power and acquired using PMT detector and an emission filter range from 578-696nm for mCherry detection. We acquired a stack of 512 raster-scanned frames for each field. The size of the images was 256×256 pixels. The pixel dwell time was 1.58μs/pixel. The stack of 512 images was acquired in about 2 minutes.The acquired N&B images were processed by the SimFCS software developed by Laboratory for Fluorescence Dynamics (LFD) at University of California, Irvine. The brightness of mCherry protein was measured for the calibration of the monomeric protein brightness.

5.3 Result

To measure the brightness of monomers, we performed N&B analysis on HEK293 cells transfected with monomeric mCherry alone. The result shows that the majority of the protein was in the monomeric form represented by green pixels in figure 5.3. Only very few dimers were observed (red pixels). The apparent brightness of monomers, dimers, and tetramers are at 1.084, 1.189, and 1.378 respectively.

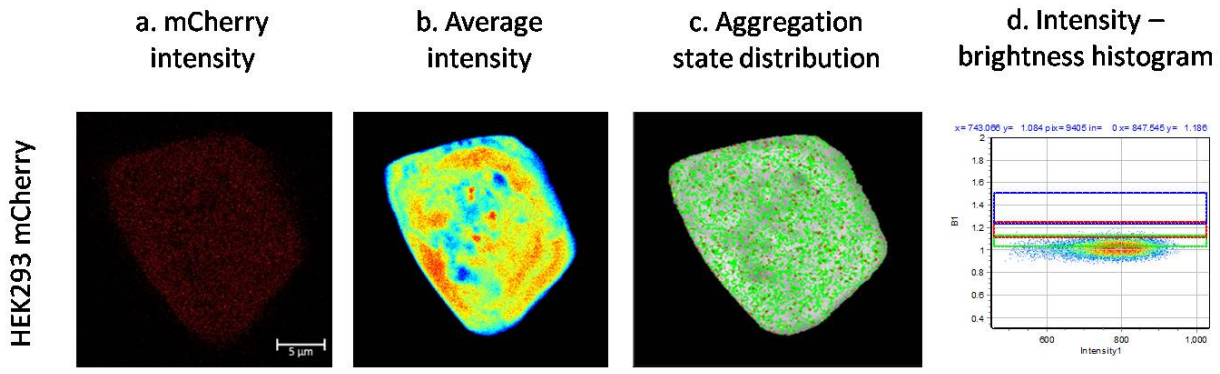

Figure 5.3: N&B analysis of HEK293 mCherry cells. (a) mCherry intensity image excited at 561nm acquired in the red channel. (Scale bar: 5µm) (b) Average fluorescence intensity map of HEK293 cells transfected with mCherry. (c) Selection of the pixels with the brightness corresponding to monomers (green), dimers (red) and tetramers (blue). (d) Intensity vs. apparent brightness histogram with the noise at 1.

To test if this result is consistent in cells with unexpanded polyQ repeats, HEK293 cells were transiently transfected with Htt25Q-mCherry plasmid and imaged 24 hours after transfection. Typically, the HTT gene with no more than 35 CAG repeats does not form aggregates. In this case, mainly monomers were observed and highlighted by green in figure 5.4. An increase in the red pixels compare to the green pixels reveals an increase in the percentage of dimer population.

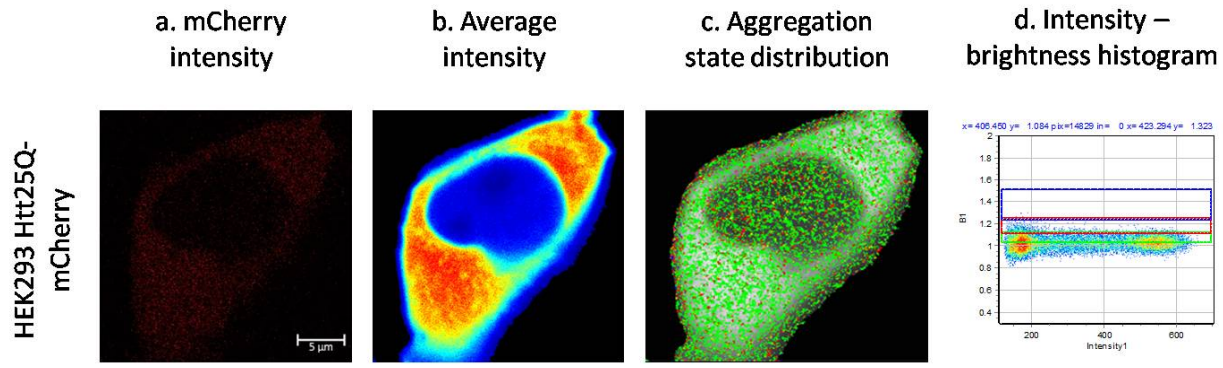

Figure 5.4: N&B analysis of HEK293 25Q-mCherry cells. (a) mCherry intensity image excited at 561nm acquired in the red channel. (Scale bar: 5µm) (b) Average fluorescence intensity map of HEK293 cells transfected with Htt25Q-mCherry plasmid. (c) Selection of the pixels with the brightness corresponding to monomers (green), dimers (red) and tetramers (blue). (d) Intensity vs. apparent brightness histogram with the noise at 1.

To determine the possible changes in the oligomerization of Htt25Q-mCherry proteins after the internalization of Htt97Q-EGFP aggregates, dishes of HEK293 Htt25Q-mCherry cells with the co-culture of Htt97Q-EGFP cells were prepared 12 hours before imaging. Htt25Q-mCherry protein expressing cells with both a medium expression level and the internalization of Htt97Q-EGFP aggregates were imaged and analyzed by N&B (Fig. 5.5). We observed a higher dimer percentage compared to mCherry and Htt25Q-mCherry in normal condition.

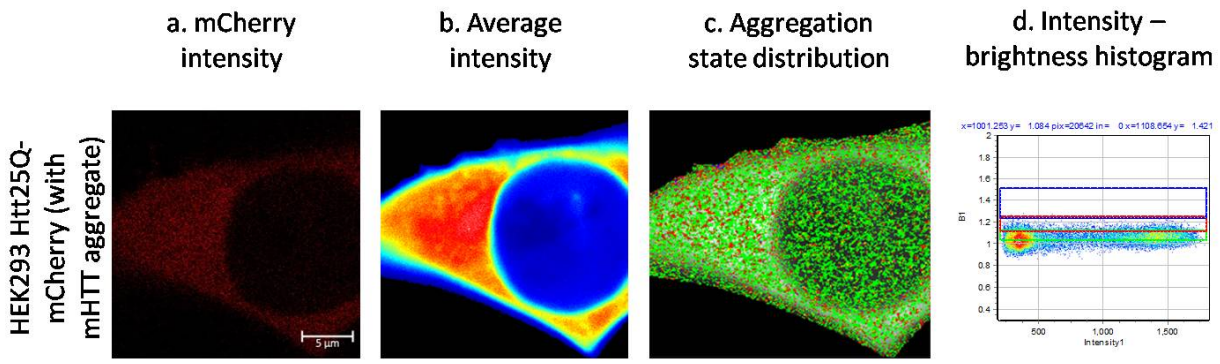

Figure 5.5: N&B analysis of HEK293 25Q-mCherry cells with the uptake of Htt97Q-EGFP aggregates. (a) mCherry intensity image excited at 561nm acquired in the red channel. (Scale bar: 5µm) (b) Average fluorescence intensity map of HEK293 Htt25Q-mCherry cells. (c) Selection of the pixels with the brightness corresponding to monomers (green), dimers (red) and tetramers (blue). (d) Intensity vs. apparent brightness histogram with the noise at 1.

Representation of monomers, dimers, and tetramers population in three different conditions is presented below. Monomers, dimers, and tetramers are represented by green, red, and blue respectively (Fig. 5.6).

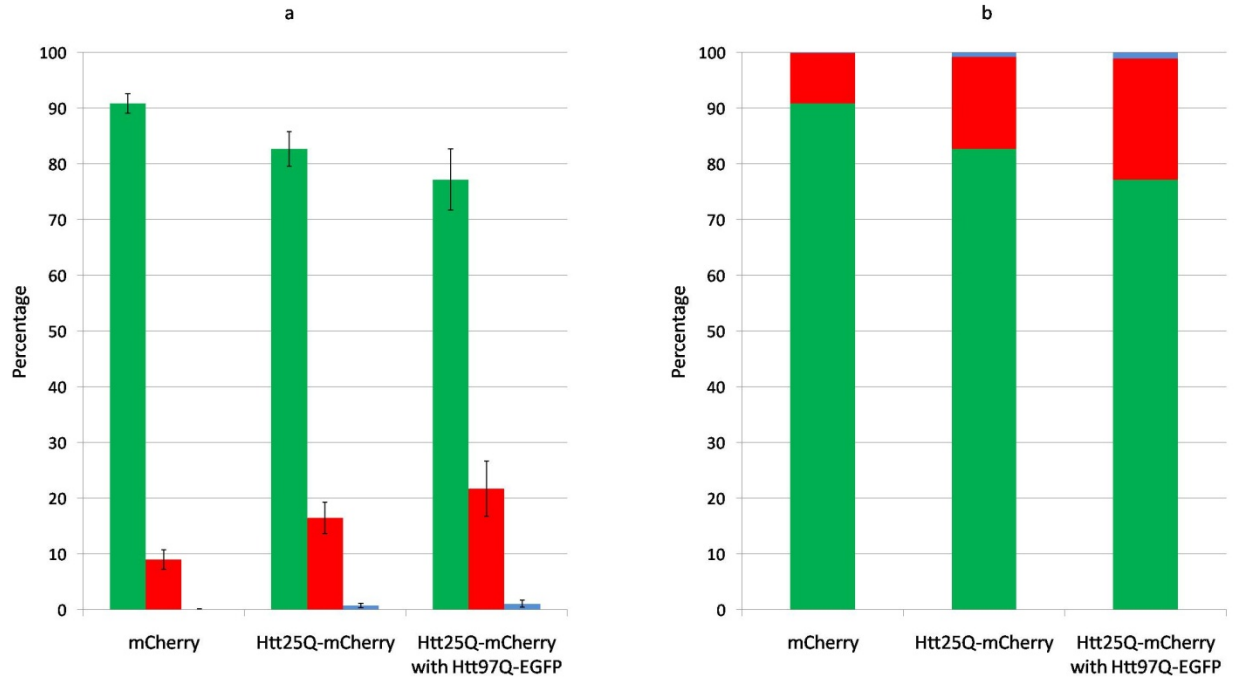

Figure 5.6: Percentage of the pixels representing monomers (green), dimers (red), and tetramers (blue) for different groups.

5.4 Discussion and Conclusion

In this work, we performed the Number and molecular Brightness (N&B) analysis to map the oligomerization in live cells induced by mHTT aggregates. As seen in the results, there is a significant increase in the percentage of oligomers, specifically dimers in cells after the internalization of extracellular mHTT aggregates. The N&B analysis of cells expressing mCherry alone shows that 90.9$\pm$1.78% of the pixels are monomers. The population of dimers is relatively low as 9.0$\pm$1.76% of the pixels are detected as dimers. There is only 0.1$\pm$0.04% of the tetramers population observed in these cells (Fig. 5.6). In contrast, when cells express Htt25Q-mCherry proteins, the percentage of monomers and dimers become 82.7$\pm$3.13% and 16.5$\pm$2.80% respectively. After the internalization of extracellular Htt97Q aggregates, the endogenous normal HTT proteins seem to be accumulated mainly in cytoplasmic region. Although different cells exhibited different rates of mCherry accumulation, the average percentage of pixels with brightness values corresponding to dimers was increased notably to 21.7$\pm$4.98% ($p < 0.05$ for all cases). No higher order aggregates or any pixel with a brightness larger than 1.5 was found in the entire experiment.

The mechanism that causes the progressive neurodegeneration in Huntington's disease is still unclear. However, evidence suggests that the internalized extracellular toxic mHTT aggregates may play an essential role in the propagation of HD. From this research, we have measured the percentage of different protein complex using N&B analysis. We found a significant decrease in the percentage of monomers and an increase in the percentage of dimers for HD healthy cells after the internalization of mHTT aggregates. Such a change may

indicate an accumulation of endogenous unexpanded HTT proteins and may provide evidence explaining the nucleating capability for the toxic mHTT aggregates in “infected” cells.

Altogether, the results show promising data on the consequence of mHTT cell-to-cell transfer in energy metabolism and aggregate formation in HD. We expect the results of this work to be a precursor for future study using neuronal cells. Further investigations are needed to apply these research methods in neuronal cells which are much more physiologically relavent to the real case. This research can be also extended to in vivo imaging of fresh brain tissue samples, which may provide much more detailed information regarding the potential consequence of mHTT transfer in live tissues. In addition, the significant metabolic shift and increased nucleating aggregates that we demonstrated here could be a powerful tool for potential HD drug screening.

BIBLIOGRAPHY

1 Brundin, P., Melki, R. & Kopito, R. Prion-like transmission of protein aggregates in neurodegenerative diseases. *Nature Reviews Molecular Cell Biology* **11**, 301 (2010).

2 Dobson, C. M. Protein folding and misfolding. *Nature* **426**, 884 (2003).

3 Hartl, F. U. & Hayer-Hartl, M. Molecular chaperones in the cytosol: from nascent chain to folded protein. *Science* **295**, 1852-1858 (2002).

4 Ciechanover, A. Proteolysis: from the lysosome to ubiquitin and the proteasome. *Nature reviews Molecular cell biology* **6**, 79 (2005).

5 DeMartino, G. N. & Gillette, T. G. Proteasomes: machines for all reasons. *Cell* **129**, 659-662 (2007).

6 Tydlacka, S., Wang, C.-E., Wang, X., Li, S. & Li, X.-J. Differential activities of the ubiquitin–proteasome system in neurons versus glia may account for the preferential accumulation of misfolded proteins in neurons. *Journal of Neuroscience* **28**, 13285-13295 (2008).

7 Kopito, R. R. Aggresomes, inclusion bodies and protein aggregation. *Trends in cell biology* **10**, 524-530 (2000).

8 Venkatraman, P., Wetzel, R., Tanaka, M., Nukina, N. & Goldberg, A. L. Eukaryotic proteasomes cannot digest polyglutamine sequences and release them during degradation of polyglutamine-containing proteins. *Molecular cell* **14**, 95-104 (2004).

9 Walker, F. O. Huntington's disease. *The Lancet* **369**, 218-228 (2007).

10 MacDonald, M. E. *et al.* A novel gene containing a trinucleotide repeat that is expanded and unstable on Huntington's disease chromosomes. *Cell* **72**, 971-983 (1993).

11 Borrell-Pages, M., Zala, D., Humbert, S. & Saudou, F. Huntington's disease: from huntingtin function and dysfunction to therapeutic strategies. *Cellular and Molecular Life Sciences CMLS* **63**, 2642-2660 (2006).

12 Foroud, T., Gray, J., Ivashina, J. & Conneally, P. M. Differences in duration of Huntington's disease based on age at onset. *Journal of Neurology, Neurosurgery & Psychiatry* **66**, 52-56 (1999).

13 Rasmussen, A. *et al.* Huntington disease in children: genotype-phenotype correlation. *Neuropediatrics* **31**, 190-194 (2000).

14 Seneca, S. *et al.* Early onset Huntington disease: a neuronal degeneration syndrome. *European journal of pediatrics* **163**, 717-721 (2004).

15 Myrianthopoulos, N. C. Huntington's Chorea. *Journal of Medical Genetics* **3**, 298-314 (1966).

16 Turpin, J. C. [Huntington chorea in children]. *Arch Fr Pediatr* **50**, 119-122 (1993).

17 Brinkman, R., Mezei, M., Theilmann, J., Almqvist, E. & Hayden, M. The likelihood of being affected with Huntington disease by a particular age, for a specific CAG size. *American journal of human genetics* **60**, 1202 (1997).

18 Vonsattel, J. P. G. & DiFiglia, M. Huntington disease. *Journal of neuropathology and experimental neurology* **57**, 369 (1998).

19 Rubinsztein, D. C. in *Genetics of Movement Disorders* 365-383 (Academic Press, 2003).

20 Lange, H., Thörner, G., Hopf, A. & Schröder, K. F. Morphometric studies of the neuropathological changes in choreatic diseases. *Journal of the Neurological Sciences* **28**, 401-425, doi:https://doi.org/10.1016/0022-510X(76)90114-3 (1976).

21 Roos, R., Bots, G. T. A. & Hermans, J. Quantitative analysis of morphological features in Huntington's disease. *Acta neurologica scandinavica* **73**, 131-135 (1986).

22 Reiner, A. *et al.* Differential loss of striatal projection neurons in Huntington disease. *Proceedings of the National Academy of Sciences* **85**, 5733-5737, doi:10.1073/pnas.85.15.5733 (1988).
23 Graveland, G., Williams, R. & DiFiglia, M. Evidence for degenerative and regenerative changes in neostriatal spiny neurons in Huntington's disease. *Science* **227**, 770-773, doi:10.1126/science.3155875 (1985).
24 Novak, M. & Tabrizi, S. J. Huntington's disease. *Bmj* **340**, c3109 (2010).
25 Ross, C. A. & Tabrizi, S. J. Huntington's disease: from molecular pathogenesis to clinical treatment. *The Lancet Neurology* **10**, 83-98, doi:https://doi.org/10.1016/S1474-4422(10)70245-3 (2011).
26 Tetrabenazine as antichorea therapy in Huntington disease. *A randomized controlled trial* **66**, 366-372, doi:10.1212/01.wnl.0000198586.85250.13 (2006).
27 Savani, A. A. & Login, I. S. Tetrabenazine as antichorea therapy in Huntington disease: a randomized controlled trial. *Neurology* **68**, 797-797 (2007).
28 Martin, B. *et al.* Therapeutic perspectives for the treatment of Huntington's disease: treating the whole body. *Histology and histopathology* **23**, 237 (2008).
29 Southwell, A. L., Ko, J. & Patterson, P. H. Intrabody gene therapy ameliorates motor, cognitive, and neuropathological symptoms in multiple mouse models of Huntington's disease. *Journal of Neuroscience* **29**, 13589-13602 (2009).
30 Young, A. B. Huntingtin in health and disease. *The Journal of clinical investigation* **111**, 299-302 (2003).
31 Landles, C. & Bates, G. P. Huntingtin and the molecular pathogenesis of Huntington's disease: Fourth in Molecular Medicine Review Series. *EMBO reports* **5**, 958-963 (2004).
32 Nasir, J. *et al.* Targeted disruption of the Huntington's disease gene results in embryonic lethality and behavioral and morphological changes in heterozygotes. *Cell* **81**, 811-823 (1995).
33 Duyao, M. P. *et al.* Inactivation of the mouse Huntington's disease gene homolog Hdh. *Science* **269**, 407-410 (1995).
34 Zeitlin, S., Liu, J.-P., Chapman, D. L., Papaioannou, V. E. & Efstratiadis, A. Increased apoptosis and early embryonic lethality in mice nullizygous for the Huntington's disease gene homologue. *Nature genetics* **11**, 155 (1995).
35 Li, W., Serpell, L. C., Carter, W. J., Rubinsztein, D. C. & Huntington, J. A. Expression and characterization of full-length human huntingtin, an elongated HEAT repeat protein. *Journal of Biological Chemistry* **281**, 15916-15922 (2006).
36 Takano, H. & Gusella, J. F. The predominantly HEAT-like motif structure of huntingtin and its association and coincident nuclear entry with dorsal, an NF-kB/Rel/dorsal family transcription factor. *BMC neuroscience* **3**, 15 (2002).
37 Li, S.-H. & Li, X.-J. Huntingtin–protein interactions and the pathogenesis of Huntington's disease. *TRENDS in Genetics* **20**, 146-154 (2004).
38 Davies, S. W. *et al.* Formation of Neuronal Intranuclear Inclusions Underlies the Neurological Dysfunction in Mice Transgenic for the HD Mutation. *Cell* **90**, 537-548, doi:https://doi.org/10.1016/S0092-8674(00)80513-9 (1997).
39 Hackam, A. S. *et al.* The Influence of Huntingtin Protein Size on Nuclear Localization and Cellular Toxicity. *The Journal of Cell Biology* **141**, 1097-1105, doi:10.1083/jcb.141.5.1097 (1998).
40 Schilling, G. *et al.* Intranuclear Inclusions and Neuritic Aggregates in Transgenic Mice Expressing a Mutant N-Terminal Fragment of Huntingtin. *Human Molecular Genetics* **8**, 397-407, doi:10.1093/hmg/8.3.397 (1999).
41 Harjes, P. & Wanker, E. E. The hunt for huntingtin function: interaction partners tell many different stories. *Trends in biochemical sciences* **28**, 425-433 (2003).

42 Steffan, J. S. *et al.* SUMO Modification of Huntingtin and Huntington's Disease Pathology. *Science* **304**, 100-104, doi:10.1126/science.1092194 (2004).
43 DiFiglia, M. *et al.* Huntingtin is a cytoplasmic protein associated with vesicles in human and rat brain neurons. *Neuron* **14**, 1075-1081, doi:https://doi.org/10.1016/0896-6273(95)90346-1 (1995).
44 Sharp, A. H. *et al.* Widespread expression of Huntington's disease gene (IT15) protein product. *Neuron* **14**, 1065-1074, doi:https://doi.org/10.1016/0896-6273(95)90345-3 (1995).
45 DiFiglia, M. *et al.* Aggregation of Huntingtin in Neuronal Intranuclear Inclusions and Dystrophic Neurites in Brain. *Science* **277**, 1990-1993, doi:10.1126/science.277.5334.1990 (1997).
46 Sameni, S., Malacrida, L., Tan, Z. & Digman, M. A. Alteration in Fluidity of Cell Plasma Membrane in Huntington Disease Revealed by Spectral Phasor Analysis. *Scientific reports* **8**, 734 (2018).
47 McBride, H. M., Neuspiel, M. & Wasiak, S. Mitochondria: more than just a powerhouse. *Current biology* **16**, R551-R560 (2006).
48 Zeviani, M. & Di Donato, S. Mitochondrial disorders. *Brain* **127**, 2153-2172 (2004).
49 Beal, M. F. Mitochondrial dysfunction in neurodegenerative diseases. *Biochimica et Biophysica Acta (BBA) - Bioenergetics* **1366**, 211-223, doi:https://doi.org/10.1016/S0005-2728(98)00114-5 (1998).
50 Panov, A. V. *et al.* Early mitochondrial calcium defects in Huntington's disease are a direct effect of polyglutamines. *Nature neuroscience* **5**, 731 (2002).
51 Trushina, E. *et al.* Mutant huntingtin impairs axonal trafficking in mammalian neurons in vivo and in vitro. *Molecular and cellular biology* **24**, 8195-8209 (2004).
52 Orr, A. L. *et al.* N-terminal mutant huntingtin associates with mitochondria and impairs mitochondrial trafficking. *Journal of Neuroscience* **28**, 2783-2792 (2008).
53 Saft, C. *et al.* Mitochondrial impairment in patients and asymptomatic mutation carriers of Huntington's disease. *Movement disorders* **20**, 674-679 (2005).
54 Ciammola, A. *et al.* Low anaerobic threshold and increased skeletal muscle lactate production in subjects with Huntington's disease. *Movement disorders* **26**, 130-137 (2011).
55 Gu, M. *et al.* Mitochondrial defect in Huntington's disease caudate nucleus. *Annals of Neurology: Official Journal of the American Neurological Association and the Child Neurology Society* **39**, 385-389 (1996).
56 Seong, I. S. *et al.* HD CAG repeat implicates a dominant property of huntingtin in mitochondrial energy metabolism. *Human molecular genetics* **14**, 2871-2880 (2005).
57 Zhang, S. *et al.* Impaired brain creatine kinase activity in Huntington's disease. *Neurodegenerative diseases* **8**, 194-201 (2011).
58 Burke, J. R. *et al.* Huntingtin and DRPLA proteins selectively interact with the enzyme GAPDH. *Nature medicine* **2**, 347 (1996).
59 Carmo, C., Naia, L., Lopes, C. & Rego, A. C. in *Polyglutamine Disorders* 59-83 (Springer, 2018).
60 Ferreira, I. L. *et al.* Bioenergetic dysfunction in Huntington's disease human cybrids. *Experimental neurology* **231**, 127-134 (2011).
61 Jenkins, B., Koroshetz, W., Beal, M. & Rosen, B. Evidence for impairment of energy metabolism in vivo in Huntington's disease using localized 1H NMR spectroscopy. *Neurology* **43**, 2689-2695 (1993).
62 Martin, W. W., Wieler, M. & Hanstock, C. C. Is brain lactate increased in Huntington's disease? *Journal of the neurological sciences* **263**, 70-74 (2007).
63 Lopes, C. *et al.* IGF-1 intranasal administration rescues Huntington's disease phenotypes in YAC128 mice. *Molecular neurobiology* **49**, 1126-1142 (2014).

64 Tsang, T. M. *et al.* Metabolic characterization of the R6/2 transgenic mouse model of Huntington's disease by high-resolution MAS 1H NMR spectroscopy. *Journal of proteome research* **5**, 483-492 (2006).
65 Benchoua, A. *et al.* Involvement of mitochondrial complex II defects in neuronal death produced by N-terminus fragment of mutated huntingtin. *Molecular biology of the cell* **17**, 1652-1663 (2006).
66 Klivenyi, P. *et al.* Mice deficient in dihydrolipoamide dehydrogenase show increased vulnerability to MPTP, malonate and 3‐nitropropionic acid neurotoxicity. *Journal of neurochemistry* **88**, 1352-1360 (2004).
67 Tabrizi, S. *et al.* Biochemical abnormalities and excitotoxicity in Huntington's disease brain. *Annals of Neurology: Official Journal of the American Neurological Association and the Child Neurology Society* **45**, 25-32 (1999).
68 Hartl, F. U. & Hayer-Hartl, M. Converging concepts of protein folding in vitro and in vivo. *Nature structural & molecular biology* **16**, 574 (2009).
69 Kodali, R. & Wetzel, R. Polymorphism in the intermediates and products of amyloid assembly. *Current opinion in structural biology* **17**, 48-57 (2007).
70 Clavaguera, F. *et al.* Transmission and spreading of tauopathy in transgenic mouse brain. *Nature cell biology* **11**, 909 (2009).
71 De Calignon, A. *et al.* Propagation of tau pathology in a model of early Alzheimer's disease. *Neuron* **73**, 685-697 (2012).
72 Angot, E. & Brundin, P. Dissecting the potential molecular mechanisms underlying α-synuclein cell-to-cell transfer in Parkinson's disease. *Parkinsonism & related disorders* **15**, S143-S147 (2009).
73 Ayers, J. I., Fromholt, S. E., O'Neal, V. M., Diamond, J. H. & Borchelt, D. R. Prion-like propagation of mutant SOD1 misfolding and motor neuron disease spread along neuroanatomical pathways. *Acta neuropathologica* **131**, 103-114 (2016).
74 Pearce, M. M., Spartz, E. J., Hong, W., Luo, L. & Kopito, R. R. Prion-like transmission of neuronal huntingtin aggregates to phagocytic glia in the Drosophila brain. *Nature communications* **6**, 6768 (2015).
75 Brahic, M., Bousset, L., Bieri, G., Melki, R. & Gitler, A. D. Axonal transport and secretion of fibrillar forms of α-synuclein, Aβ42 peptide and HTTExon 1. *Acta neuropathologica* **131**, 539-548 (2016).
76 Trajkovic, K., Jeong, H. & Krainc, D. Mutant huntingtin is secreted via a late endosomal/lysosomal unconventional secretory pathway. *Journal of Neuroscience*, 0118-0117 (2017).
77 Jansen, A. H., Batenburg, K. L., Pecho-Vrieseling, E. & Reits, E. A. Visualization of prion-like transfer in Huntington's disease models. *Biochimica et Biophysica Acta (BBA)-Molecular Basis of Disease* **1863**, 793-800 (2017).
78 Danzer, K. M. *et al.* Exosomal cell-to-cell transmission of alpha synuclein oligomers. *Molecular neurodegeneration* **7**, 42 (2012).
79 Chai, Y.-J. *et al.* The secreted oligomeric form of α‐synuclein affects multiple steps of membrane trafficking. *FEBS letters* **587**, 452-459 (2013).
80 Bieri, G., Gitler, A. D. & Brahic, M. Internalization, axonal transport and release of fibrillar forms of alpha-synuclein. *Neurobiology of disease* **109**, 219-225 (2018).
81 Babcock, D. T. & Ganetzky, B. Transcellular spreading of huntingtin aggregates in the Drosophila brain. *Proceedings of the National Academy of Sciences* **112**, E5427-E5433 (2015).
82 Ren, P.-H. *et al.* Cytoplasmic penetration and persistent infection of mammalian cells by polyglutamine aggregates. *Nature cell biology* **11**, 219 (2009).

83 Victoria, G. S. & Zurzolo, C. The spread of prion-like proteins by lysosomes and tunneling nanotubes: implications for neurodegenerative diseases. *J Cell Biol*, jcb. 201701047 (2017).
84 Costanzo, M. *et al.* Transfer of polyglutamine aggregates in neuronal cells occurs in tunneling nanotubes. *J Cell Sci*, jcs. 126086 (2013).
85 Pecho-Vrieseling, E. *et al.* Transneuronal propagation of mutant huntingtin contributes to non–cell autonomous pathology in neurons. *Nature neuroscience* **17**, 1064 (2014).
86 Sameni, S., Syed, A., Marsh, J. L. & Digman, M. A. The phasor-FLIM fingerprints reveal shifts from OXPHOS to enhanced glycolysis in Huntington Disease. *Scientific reports* **6**, 34755 (2016).
87 Weber, G. Fluorescence and phosphorescence analysis. *Interscience, New York*, 217-240 (1966).
88 Datta, R. *Label-free fluorescence lifetime imaging microscopy (FLIM) to study metabolism and oxidative stress in biological systems*, UC Irvine, (2016).
89 Spencer, R. D. & Weber, G. Measurements of subnanosecond fluorescence lifetimes with a cross‐correlation phase fluorometer. *Annals of the New York Academy of Sciences* **158**, 361-376 (1969).
90 Verveer, P. J., Squire, A. & Bastiaens, P. I. Global analysis of fluorescence lifetime imaging microscopy data. *Biophysical Journal* **78**, 2127-2137 (2000).
91 Gratton, E., Breusegem, S., Sutin, J. D., Ruan, Q. & Barry, N. P. Fluorescence lifetime imaging for the two-photon microscope: time-domain and frequency-domain methods. *Journal of biomedical optics* **8**, 381-391 (2003).
92 Digman, M. A., Caiolfa, V. R., Zamai, M. & Gratton, E. The phasor approach to fluorescence lifetime imaging analysis. *Biophysical journal* **94**, L14-L16 (2008).
93 Belenky, P., Bogan, K. L. & Brenner, C. NAD+ metabolism in health and disease. *Trends in biochemical sciences* **32**, 12-19 (2007).
94 Bird, D. K. *et al.* Metabolic mapping of MCF10A human breast cells via multiphoton fluorescence lifetime imaging of the coenzyme NADH. *Cancer Research* **65**, 8766-8773 (2005).
95 Zipfel, W. R. *et al.* Live tissue intrinsic emission microscopy using multiphoton-excited native fluorescence and second harmonic generation. *Proceedings of the National Academy of Sciences* **100**, 7075-7080 (2003).
96 Trinh, A. L. *et al.* Tracking Functional Tumor Cell Subpopulations of Malignant Glioma by Phasor Fluorescence Lifetime Imaging Microscopy of NADH. *Cancers* **9**, 168 (2017).
97 Stringari, C., Sierra, R., Donovan, P. J. & Gratton, E. Label-free separation of human embryonic stem cells and their differentiating progenies by phasor fluorescence lifetime microscopy. *Journal of biomedical optics* **17**, 046012 (2012).
98 Stringari, C., Nourse, J. L., Flanagan, L. A. & Gratton, E. Phasor fluorescence lifetime microscopy of free and protein-bound NADH reveals neural stem cell differentiation potential. *PloS one* **7**, e48014 (2012).
99 Mah, E. J., McGahey, G. E., Yee, A. F. & Digman, M. A. Collagen stiffness modulates MDA-MB231 cell metabolism through adhesion-mediated contractility. *bioRxiv*, 272948 (2018).
100 Ma, N., Digman, M. A., Malacrida, L. & Gratton, E. Measurements of absolute concentrations of NADH in cells using the phasor FLIM method. *Biomedical optics express* **7**, 2441-2452 (2016).
101 Ossato, G. *Protein aggregation in neurodegenerative disease*. (University of California, Irvine, 2010).
102 Digman, M. A., Dalal, R., Horwitz, A. F. & Gratton, E. Mapping the number of molecules and brightness in the laser scanning microscope. *Biophysical journal* **94**, 2320-2332 (2008).